



## Structure, degradation, drug release and mechanical properties relationships of iron-based drug eluting scaffolds: The effects of PLGA

Abdul Hakim Yusop <sup>a</sup>, Murni Nazira Sarian <sup>b</sup>, Fatihhi Szali Januddi <sup>c</sup>, Qamar Uddin Ahmed <sup>b</sup>, Mohammed Rafiq Kadir <sup>a</sup>, Djoko Hartanto <sup>d</sup>, Hendra Hermawan <sup>e,\*</sup>, Hadi Nur <sup>f,g,\*\*</sup>

<sup>a</sup> Medical Devices Technology Group (MediTeg), Faculty of Biosciences and Medical Engineering, Universiti Teknologi Malaysia, Johor Bahru 81310, Malaysia

<sup>b</sup> Department of Pharmaceutical Chemistry, Kulliyah of Pharmacy, International Islamic University Malaysia, Kuantan 25200, Malaysia

<sup>c</sup> Universiti Kuala Lumpur, Malaysian Institute of Industrial Technology, Johor Bahru 81750, Malaysia

<sup>d</sup> Department of Chemistry, Institut Teknologi Sepuluh Nopember, Jawa Timur 60111, Indonesia

<sup>e</sup> Department of Mining, Metallurgical and Materials Engineering & CHU de Québec Research Center, Laval University, Quebec G1V0A6, Canada

<sup>f</sup> Center for Sustainable Nanomaterials, Ibnu Sina Institute for Scientific and Industrial Research, Universiti Teknologi Malaysia, Johor Bahru 81310, Malaysia

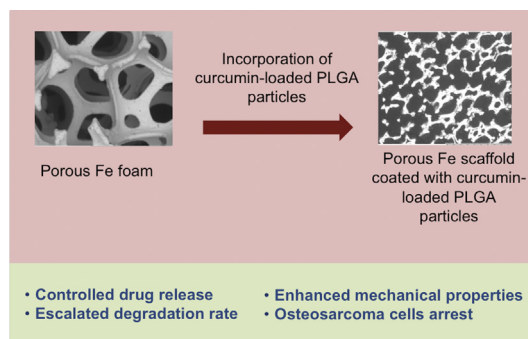
<sup>g</sup> Central Laboratory of Minerals and Advanced Materials, Faculty of Mathematics and Natural Sciences, State University of Malang, Malang 65145, Indonesia



### HIGHLIGHTS

- The incorporation of the curcumin-loaded PLGA in the iron porous structure
- Degradation of porous iron in the presence of poly(lactic-co-glycolic acid)
- Structure, degradation, drug release and mechanical properties relationships
- PLGA-iron interfacial interaction enhanced the degradation
- The drug device as an integrated system for favorable scaffold-based drug design

### GRAPHICAL ABSTRACT



### ARTICLE INFO

#### Article history:

Received 11 June 2018

Received in revised form 21 August 2018

Accepted 10 September 2018

Available online 12 September 2018

#### Keywords:

PLGA

Porous iron

Iron degradation

Curcumin release

Bone cancer scaffolds

### ABSTRACT

The effects of poly(lactic-co-glycolic acid) (PLGA) on structure, degradation, drug release and mechanical properties relationships of iron-based drug eluting scaffolds have been studied comprehensively. The porous structure of the iron has been incorporated with the curcumin-loaded PLGA (CP) particles through dipping method to produce CP-coated porous Fe (CP-Fe). The CP-Fe degradation has been escalated with the increase of PLGA composition due to the hydrolysis of PLGA. The degradation of iron substrate triggered the kinetics of curcumin release as there was a direct correlation between the curcumin release rate and the degradation rate of the CP-Fe scaffold. The stiffness of the CP particles and the interfacial interactions developed between the CP coating and iron surface have enhanced scaffolds' mechanical strengths. The curcumin released from the scaffold significantly arrested osteosarcoma cells growth. It is demonstrated that the PLGA played an important role to control the scaffold degradation and curcumin release as well as enhancing the mechanical properties of the drug device as an integrated system for favorable scaffold-based drug design.

© 2018 Published by Elsevier Ltd. This is an open access article under the CC BY-NC-ND license (<http://creativecommons.org/licenses/by-nc-nd/4.0/>).

\* Corresponding author.

\*\* Correspondence to: H. Nur, Center for Sustainable Nanomaterials, Ibnu Sina Institute for Scientific and Industrial Research, Universiti Teknologi Malaysia, Johor Bahru 81310, Malaysia.

E-mail addresses: [hendra.hermawan@gmn.ulaval.ca](mailto:hendra.hermawan@gmn.ulaval.ca) (H. Hermawan), [hadi@kimia.fs.utm.my](mailto:hadi@kimia.fs.utm.my)

URL: <http://hadinur.com> (H. Nur).

## 1. Introduction

A drug-device system offers a higher efficiency on the dose control over a specific targeted tissue and reduces the side effects to non-targeted tissues as compared to the systemic drug delivery method [1]. Medical implants are often used as the vehicle for that kind of system such as an absorbable drug eluting stent that releases anti-proliferative drug on smooth muscle cells [2], and a bone scaffold that delivers anticancer drugs [3]. The porous structure of the scaffold can be loaded with anti-cancer agents to simultaneously provide tumour therapeutic effect while stimulate bone formation.

Porous biodegradable metals have been studied as new materials for bone scaffolds due to their combination of strength and ductility where polymer or ceramic are unable to provide it [4–6]. The use of biodegradable metals acting as temporary implants could abrogate the necessity of second removal surgery and could circumvent the long-term negative effects of permanent implantation [7]. The advancing additive manufacturing technology helps to enhance the design and process of ideal topological porous metals suited for bone scaffolds [8,9]. Porous magnesium was among the first absorbable metals studied for bone scaffolds. Poly(caprolactone), poly(lactic-co-glycolic acid) (PLGA) and bioglass were integrated into the porous magnesium to enhance its bioactivity, degradation resistance, mechanical stability and to balance the elevated pH due to magnesium degradation [10–13]. However, magnesium scaffolds face a challenge as the high surface area of porous structure increases the degradation rate, despite various methods used to control it [6,12,14]. Porous zinc showed a better degradation resistance in simulated body fluid than magnesium and it had the ability to induce CaP precipitation but was suggested for low load bearing bone scaffolds due to its low strength [15]. Compared to magnesium and zinc, iron has a higher strength and slower degradation which gives a higher degree of freedom in varying its porous structure for controlling the degradation rate and matching the different strength and flexibility requirement for bone scaffolds [16,17].

Current studies on porous Fe and its alloys reported that their mechanical properties were in the range of those of natural bones [9,18] and showing encouraging biocompatibility towards osteoblast cells and human blood [9,19]. Nevertheless, these promising findings have been hampered by its slow degradation rate that makes it unmatched with the tissue-healing period [20]. Various attempts have been performed to improve the Fe degradation through alloying [9], making a composite of iron with bioceramics [21] and polymeric coating on Fe surface [22]. Porous iron was fabricated via various manufacturing routes encompassing powder metallurgy, particulate leaching, 3-D printing and replication technique [23–25]. 3D-printed Fe-Mn and Fe-Mn-1Ca constructs demonstrated a good cytocompatibility towards MC3T3 pre-osteoblasts cells and possessed a relatively higher corrosion current density compared to sintered compacted scaffolds [9]. Porous Fe/Fe-W alloy scaffolds prepared via electrodeposition showed an improved degradation rate and a mechanical strength closes to that of cancellous bone [26]. Porous Fe-Mn-Si-Pd alloys were fabricated via powder metallurgy with various degree of porosity to render suitable mechanical and magnetic properties [23]. In view of enhancing osteoconductivity and antibacterial property, pure iron foam was coated with silver containing calcium phosphate resulting into a good biominerization effect and a slow release of silver ion release for potential long-term antibacterial effect [27]. Strontium and bisphosphonate were coated on iron scaffolds for use in osteoporotic fracture defect healing. The coated scaffold greatly enhanced bone formation as compared to plain iron scaffold, but the coating did not enhance iron degradation rate [28].

Biodegradable polymers coating has been proved to increase degradation rate of iron. Poly(L-lactic acid) was coated on iron-based stents resulting into increased degradation rate without inciting any biological problem up to 13 months implantation in rabbits [22]. PLGA has been numerously employed in biomedical applications and it has functioned

commonly as a drug carrier [29] and functionalized coating agent [30]. It possesses a tuneable degradation rate and this favours its wide use as a beneficial entity in a biomedical system. It degrades through hydrolysis that produces acidic soluble monomers of lactic acid and glycolic acid. Curcumin-loaded PLGA particles have been extensively studied in various drug delivery applications [31]. Herein, we combined the curcumin-PLGA (CP) drug release system with porous iron scaffolds to produce curcumin loaded iron-based drug eluting scaffolds as a novel drug-device system for bone cancer applications. The PLGA with varied compositions have been incorporated in the curcumin loaded iron-based scaffolds and its effects on the functionalities of the drug-device system were evaluated comprehensively to demonstrate this drug device as an integrated system for favorable scaffold-based drug design.

## 2. Materials and methods

### 2.1. Materials

PLGA (lactide-to-glycolide moiety ratio of 50:50) were purchased from Lactel, USA. Porous pure iron sheets (purity = 99.9%, average relative density = 0.038, cell size of 450 µm, 88% porosity, 1.6 mm thickness) were kindly provided by Alantum, Korea. According to the manufacturer, the porous pure iron sheet was made via a polymer (polyurethane) space holder method. Poly(acrylic acid) PAA ( $M_w$  5000, Acros solution, USA), acting as surfactant were purchased from Sigma Chemical Co. (St. Louis, USA). Curcumin were purchased from Qrec, China. Acetone ( $\geq 99.5$ , ACS reagent grade) used as solvent for both curcumin and PLGA were purchased from Qrec, China.

### 2.2. Sample preparation

The curcumin-loaded PLGA particles (CP) were fabricated using single emulsion-solvent evaporation method with slight modifications [32]. Briefly, 80 mg PLGA were dissolved in 30 mL acetone under constant stirring at 500 rpm for 30 min to get a uniform solution. To this solution, 320 mg curcumin dissolved in 20 mL acetone was added and stirred for about 20 min at 500 rpm. An aqueous solution of PAA (0.5% w/v) acting as an emulsifier was slowly poured into the organic phase and stirred at 500 rpm for 30 min. The emulsion was then evaporated overnight under magnetic stirring at room temperature to evaporate the solvent. The CP particles were collected by ultracentrifugation at 10000 rpm for 20 min (Universal Centrifuge, Model 5922, Kubota). The CP pellets produced were rinsed once gently with distilled water to remove the undesired excess surfactant agglomerations from the resultant pellet. Then the CP pellets were freeze-dried for 48 h using a freeze-dryer (Christ, Germany). Three different groups of CP particles with different curcumin-PLGA weight compositions have been prepared. The prepared 80C-20P, 50C-50P and 20C-80P samples represented 80 wt% curcumin-20 wt% PLGA, 50 wt% curcumin-50 wt% PLGA and 20 wt% curcumin-80 wt% PLGA, respectively.

A dipping method was used to coat the CP particles on the porous iron. A study was conducted to determine the optimum concentration of CP that gives the highest coating deposition. 5 different CP concentrations were varied; 300, 400, 500, 600 and 700 mg/mL. The CP solution was prepared by dissolving CP particles in acetone under constant stirring at 100 rpm for 5 min. Then, the porous iron samples (6 mm × 6 mm × 1.6 mm dimension) were hang by threads and completely dipped into the CP solution for 3 min at room temperature. The CP-coated porous irons (CP-Fe) were taken out and were let to dry for 72 h at room temperature. The weights after coating were determined by an analytical balance (Shimadzu, model ATY 124).

### 2.3. Physical characterizations of CP particles and CP-Fe scaffolds

500 µL of the CP suspension were dropped on a 2 mm-thick stainless steel plate and were kept dried for 24 h at room temperature. Prior to

FESEM observation, the dried CP samples were sputter-coated with platinum (Q150R S model, Quorum, UK). The FESEM observations were performed at 2 kV voltage. Besides, the coating infiltrations were also examined using Scanning Electron Microscope (Table-top SEM, Hitachi). The cross-sections of the coated scaffolds were prepared by cutting the scaffolds with a sharp razor blade in liquid nitrogen [33].

#### 2.4. Interfacial interactions by XPS and ATR-FTIR analyses

For ATR-FTIR analysis, infrared absorbance spectra were obtained with 32 scans per sample over the range of 500–4000 cm<sup>-1</sup> and then subtracted from the background ratios and plotted using OriginPro (OriginLab, USA). Three repetitions were performed for each sample to get a reproducible result. XPS spectra were recorded with use of monochromated Al K $\alpha$  excitation at a pass energy of 80 eV for survey spectra and 20 eV for the core-level and valence band spectra. Spectra are decomposed with the CasaXPS peakfit software (version 2.3.15, Casa Software Ltd., UK). The signals of high-resolution spectra were deconvoluted at full width at half maximum (FWHM) of <1.5. A Gaussian/Lorentzian product function peak shape model GL(30) (70% Gaussian, 30% Lorentzian) was used in combination with a Shirley background.

#### 2.5. Long-term drug release study

The amounts of curcumin incorporated in the CP-Fe scaffolds were determined prior to the release study. The Cur-Fe and CP-Fe samples were immersed in 40 mL acetone in a centrifuge tube. The immersed samples were subjected to a constant agitation of 100 rpm for 15 min to leach out the curcumin into acetone [34,35]. Then, the solutions were centrifuged at 6000 rpm for 3 min, and the supernatant was collected for absorbance determination at the wavelength of  $\lambda = 425$  nm. The drug release test was performed using sample-and-separate method, as have been used widely in previous studies [36]. CP-Fe samples ( $2 \times 2 \times 2$  mm<sup>3</sup> in dimension) were immersed in 14 mL PBS solution at physiological pH of 7.4 in a centrifuge tube under constant shaking in a water bath at 100 rpm and at 37 °C. PBS is one of the common simulated body fluid and it is used to simulate the biological solution due to its ion concentrations which closely match those of the human body and non-toxic medium to living cells [37]. It contains sodium hydrogen phosphate (2.89 g/L Na<sub>2</sub>HPO<sub>3</sub>), sodium chloride (8.1 g/L NaCl), potassium chloride (0.2 g/L KCl) and potassium dihydrogen phosphate (0.2 g/L KH<sub>2</sub>PO<sub>3</sub>) [38]. It is suitable for long-term in vitro biological evaluation [39,40]. At predetermined time interval, 1 mL aliquot of the solution was withdrawn using a micropipette for absorbance analysis to measure the released curcumin; then 1 mL of fresh PBS was added to replenish and to maintain the total dissolution volume. The amount of curcumin released was measured spectroscopically in a 96-well plate via a microplate photometer (Multiskan FC, Thermo Scientific, US) at 425 nm wavelength. Pure Fe, pure PLGA and PLGA-Fe were employed as controls. Five samples from each group were tested. The cumulative releases of the curcumin are determined based on the daily releases.

#### 2.6. Degradation tests

##### 2.6.1. Potentiodynamic polarization (PDP) test

Prior to the PDP test, pure Fe samples were subjected to surface finishing by mechanical grinding using silicon carbide SiC papers (#1200) followed by polishing using alumina suspension (0.3 µm, Presi, France) and polishing cloth. Then the polished Fe samples were coated with the CP using the same optimum parameters obtained earlier. The coated Fe samples (CP-Fe) were cold-mounted in acrylic resin and were attached with copper wires. The coated scaffolds were then dried at ambient temperature for 72 h. The PDP test was conducted using a potentiostat (Versastat 3, Princeton Applied Research, USA)

and deploying a standard three-electrode system in 250 mL PBS solution with graphite rod as the auxiliary and Ag/AgCl (NaCl, 3.5 M) as the reference electrodes. The tested samples having a nominal exposed surface area of 1.0 cm<sup>2</sup> deployed as the working electrode. The tests were conducted at 37 ± 0.5 °C with a scan rate of 1.0 mV/s over a potential range of -0.25 V to 0.25 V after a 10-minute open circuit potential (OCP) run. Pure Fe, Cur-Fe, 80C-20P-Fe, 50C-50P-Fe and 20C-80P-Fe samples were tested. The determinations of corrosion potential (E<sub>corr</sub>) and corrosion current density (i<sub>corr</sub>) were in accordance with ASTM G102-89(2015) standard [41]. The degradation rates of the samples were determined based on the ASTM G59 standard with the aid of electrochemical software (EC-Lab V11.01, BioLogic, France). Five samples from each group were tested and the tests were repeated twice to obtain reproducible results.

##### 2.6.2. Weight loss measurement

Static immersion test was performed on pure Fe, Cur-Fe, 80C-20P-Fe and PLGA-Fe samples where each 5 specimens ( $6 \times 6 \times 1.6$  mm in dimension) were immersed in 14 mL PBS solution in a 15-mL glass beaker. The temperature was maintained at 37 ± 0.5 °C by placing the beakers in an isothermal water bath. Weight loss was measured at week 1, 2, 3 and 4 on 5 specimens from each group. At the predetermined times, the specimens were taken out and rinsed in deionized water then underwent mechanical cleaning through a gentle brushing using a soft brush to remove the degradation products. Then the samples were subjected to further cleaning by immersing the samples in 20 mL deionized water with the aid of 0.1% v/v nitric acid in ultrasonic bath at 37 °C for 1 min in accordance with the ASTM G31, ISO 8407:2009 and ASTM G1-03(2011) standards [42,43]. Then, the samples were dried in vacuum for 30 min followed by drying in an oven for 15 min at 40 °C. The specimens were allowed to cool in a desiccator to the room temperature for 10 min before weighing. The final weights of the dried specimen then were measured by an analytical balance (Shimadzu, model ATY 124). The weight losses of the samples were computed as the difference between the initial weight and the final weight of the samples. In addition, ATR-FTIR analysis was also performed on the dried samples to investigate the PLGA hydrolysis that occurred on the degraded scaffolds.

##### 2.6.3. Effect of PLGA on CP's conductivity

The 80C-20P, 50C-50C, 40C-60P and 20C-80P particles were cold-pressed at 3000 psi using a hydraulic press (E-Z Press™, ICL, USA) producing pellets with 1.0 mm in thickness and 13.0 mm in diameter. Then the pellets were attached to a copper wire and cold-mounted using acrylic resin. The ability of PLGA to promote ionic conductivity was assessed by electrochemical impedance spectroscopy (EIS) technique. The samples were immersed in 250 mL PBS solution and the test was carried out using a standard three-electrode system as in the PDP test with graphite rod as the auxiliary and Ag/AgCl (NaCl, 3.5 M) as the reference electrodes. The samples acted as working electrodes have 1.13 cm<sup>2</sup> exposed area. VersaStudio software (Princeton Applied Research, USA) was used for data acquisition at open circuit potential over a frequency range of 100 kHz down to 10 mHz using a peak-to-peak 10 mV sinusoidal perturbation. Lower absolute impedance is indicative of the improved ionic conductivity. The electrical conductivity of the pellets was measured using a linear four-point probe conductivity cell with uniform 2.0 mm spacing between probes. A source meter (Keithley Instruments, USA) was used to apply currents of 0.01, 0.1, 0.5, 1.0 and 1.5 nA to the pure curcumin and CP pellets and then the corresponding voltage were measured. Then, the I-V curves were constructed and the resistance was determined based on the curve. The conductivity of the CP pellets was quantified based on the obtained resistance and samples' cross-sectional area and length.

##### 2.6.4. Electrochemical impedance spectroscopy (EIS)

The EIS experiments were performed to evaluate the coating behaviour towards iron degradation over immersion time. The samples were

immersed in 10 mL PBS solution and were taken out at the predetermined time intervals to be tested via EIS. Three different groups were tested; pure Fe, Cur-Fe and 80C-20P-Fe. Five samples from each group were tested in 250 mL of PBS solution at 37 °C for 30 min per run. VersaStudio software (Princeton Applied Research, USA) was used for data acquisition at open circuit potential over a frequency range of 100 kHz down to 10 mHz using a peak-to-peak 10 mV sinusoidal perturbation. The charge transfer resistance,  $R_{ct}$  and the absolute impedance at the minimum frequency, ( $|Z|$ ) were determined from the Nyquist plot and Bode plot respectively with the aid of an EIS software (ZSimpWin version 3.6, Echem Software, USA). The measured spectra were then fitted with equivalent circuits by using the software.

#### 2.6.5. Finite-element simulation on the degradation of the CP-Fe scaffolds

The finite-element simulation was conducted to evaluate and to compare the degradation behaviour of Cur-Fe and 80C-20P-Fe scaffolds. It was performed using the commercial COMSOL® Multiphysics software (COMSOL Multiphasic, Burlington, USA, version 3.4) coupled with a programming software of MATLAB (MathWorks®, USA). The governing physics related to the degradation were firstly solved through programmings by solving the related differential equations through the MATLAB software. The equations integration extracted from the programming was then used in the COMSOL's direct coupled linear solvers to estimate the current density distributions on the surface of the coatings and the degraded iron. The scaffolds were modeled using a three-dimensional (3-D) geometry consisting of a 100 μm thick coating layer (10 mm × 10 mm in dimension) covering the 1.6-mm-thick iron scaffold layer (10 mm × 10 mm in dimension) surrounded by a region of PBS electrolyte. Infinite electrolyte was assigned in this study and the coating layers were assumed homogenous. The modeling and the simulation were performed based on the Butler-Volmer kinetics considering the coating conductivity, electrolyte conductivity, iron exchange current density and equilibrium potential of iron as the electrode. The overall electrochemical reaction was considered as an activation-controlled process. The iron-electrolyte interface fluxes are defined in terms of the cathodic and anodic current densities using the Butler-Volmer kinetics.

#### 2.7. Mechanical properties of the CP-Fe scaffolds

The mechanical properties of the CP-Fe and pure Fe samples (10 mm × 10 mm × 1.6 mm) were assessed through a uniaxial compression test using a universal testing machine (Instron 8874, Instron, USA) with a 50 kN load cell at 0.08 mm/s cross-head speed. Prior to the testing, little surface finishes were gently performed on the dried samples using SiC paper (# 1200) to produce a more uniform and flat surface. Then the samples were air-dried by air-blow using an air-compressor and let them to dry at room temperature. The test and the determination of compressive strength and stiffness values were done by following the ASTM D1621—16 and ISO 844:2014 standards. The compressive strengths were computed as the first maxima of the stress-strain curve while the values of the stiffness were measured as the slope of the stress-strain curve in the elastic deformation region. In order to assess the effect of curcumin-PLGA compositions on the mechanical properties, 80C-20P-Fe, 50C-50P-Fe, 20C-80P-Fe and Cur-Fe samples were tested. Five replicates were performed in this mechanical test. A part from that, a further study to explore the effect of CP particles' stiffness on the scaffolds strength was conducted. For this purpose, pure curcumin, 80C-20P and 20C-80P particles were tested. 500 mg/mL solution of each tested group were prepared and then dropped onto glass slides. The particles on the glass sides were let to dry in room temperature for 72 h prior to the AFM measurement. The stiffness of the particles were determined through force spectroscopy from Atomic Force Spectroscopy (AFM) measurement using QI™ tapping mode at approximately 270 kHz resonance frequencies and 2 Hz scan rates. The measurements were performed at five different spots of the samples and

the average stiffness was determined from the retraction curve of the force-distance curve obtained. Additionally, the mechanical strengths of the CP-Fe scaffolds after 28 days of immersion were also determined. Three groups of samples were tested; Cur-Fe, 80C-20P-Fe and 50C-50P-Fe samples. The tested samples were pre-immersed in 14 mL of PBS solution for 28 days. After 28 days of immersion, the samples were taken out and air-dried by an air-blow using an air-compressor and let them dry in a desiccator for 2 h prior to the test.

#### 2.8. In vitro cell viability evaluation of CP-Fe scaffolds

To evaluate anti-cancer activity of the CP-Fe scaffolds, a set of cell viability test was performed by applying direct contact according to Shearier et al. [44] method with slight modifications towards human osteosarcoma (OS) MG-63 cancer cell lines through the 3-(4,5-dimethylthiazol-2-yl)-2,5-diphenyltetrazolium bromide (MTT) assay. All scaffolds were sterilized under UV radiation for 1 h prior. The OS cells were seeded in 24-well plates ( $1.0 \times 10^5$  cells/mL medium) using RPMI media (Gibco, Thermo Fisher Scientific, USA) contained 5% of Penicillin-Streptomycin solution and 10% of fetal bovine serum (FBS) in the humidified atmosphere with 5% CO<sub>2</sub> at 37 °C for 24 h to allow cell attachment, and then directly treated with Cur-Fe and 80C-20P-Fe samples ( $2 \times 2 \times 1.6$  mm<sup>3</sup> in dimension) using Millicell® single-well inserts (Millipore, Merck, Germany) in each well to hold the scaffold at predetermined time of 7, 14, 21 and 28 days. The medium was replaced for every 3 days. Non-treated cell, pure PLGA, pure Fe and pure curcumin were treated as controls. After each predetermined day, the media and the scaffolds were discarded, then 100 μL MTT solution was added and incubated for 4 h. Then, 1 mL dimethyl sulfoxide was added in each well to dissolve the formazan crystal and further incubated for 1 h. Five samples from each group were tested. The absorbance values of the MTT solution treated with CP scaffolds were compared with that of MTT solution without scaffolds (untreated control) to obtain the percentage of cell viability values. The percentage of cell viability results were expressed as the mean value in triplicated with corresponding standard deviation. One-way ANOVA with post-hoc analysis at p-value of 0.05 and 0.01 was performed to determine the significant difference of cells viability through Tukey's HSD (honest significant difference) test [45].

#### 2.9. Statistical analysis

All data are expressed as the means ± standard deviations (SD) ( $n = 3\text{--}5$ ) in this study. Statistical comparisons were performed using one-way ANOVA through Tukey's HSD (honest significant difference) test, wherever necessary. A  $p < 0.05$  was considered statistically significant, and a  $p < 0.01$  was considered very statistically significant.

### 3. Results and discussion

#### 3.1. Surface morphology and physical properties

**Fig. 1(a)** below shows the images of curcumin-loaded PLGA (CP) particles viewed under FESEM microscopy. From the figure, it can be observed that the CP particles have sphere-like morphology and some CP particles tend to agglomerate with each other. Based on CP concentration study (data not shown), CP's concentration of 500 mg/mL gave the highest coating deposition compared to those of other tested concentrations. **Fig. 1(b)** shows the surface morphology of CP-coated porous Fe (CP-Fe) scaffolds at 500 mg/mL of CP's concentration. Based on the figure, it is evidently seen that the CP particles' distribution is uniform after being coated on the porous Fe surface. **Fig. 1(c)** depicts the cross-sectional view of the CP-Fe scaffolds whereby the CP coating

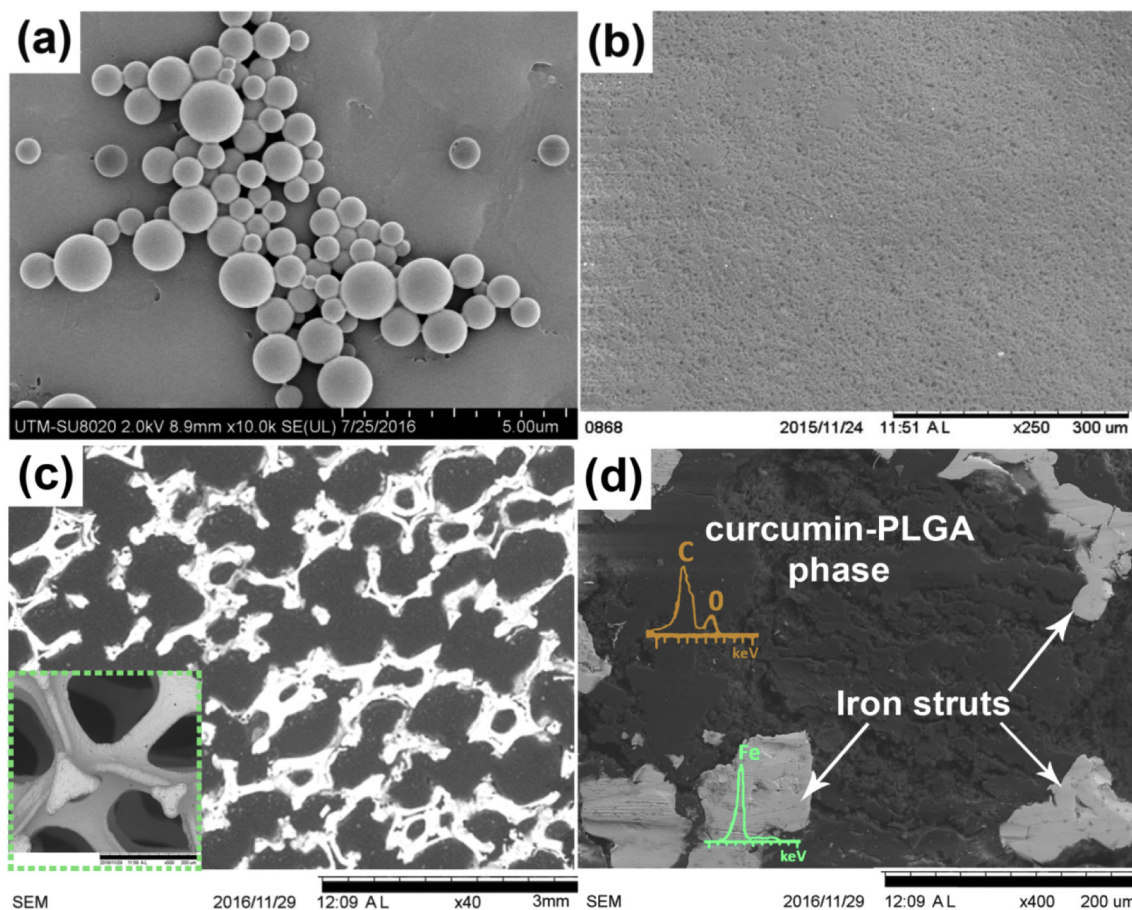


**Fig. 1.** SEM micrographs of (a) CP particles, (b) CP-Fe surface, (c) cross-section of CP-Fe at 500 mg/mL of CP concentration and the inset, reveals the bare (uncoated) structure of pure Fe scaffolds, and (d) cross-sectional view of the scaffold at higher magnification.

was seen to infiltrate the pores of the porous Fe. The inset in Fig. 1(c) depicts the SEM image of bare porous Fe without CP coating while Fig. 1(d) shows the cross-sectional view of the CP-Fe scaffold at higher magnification. As can be seen from the figure, the grey coloured phase corresponds to the CP coating while the white coloured phase represents the porous Fe struts.

The XRD and FTIR analyses of the CP particles were depicted in Supplemental Fig. S1. The XRD results shows that the curcumin were still present in its crystalline state after being incorporated into PLGA particles. Meanwhile, the FTIR results manifested that there were interfacial interactions developed between the CP coating and Fe surface as shown by the shiftings of C=O peaks of both PLGA ( $1748\text{--}1753\text{ cm}^{-1}$ ) and curcumin ( $1502\text{--}1505\text{ cm}^{-1}$ ).

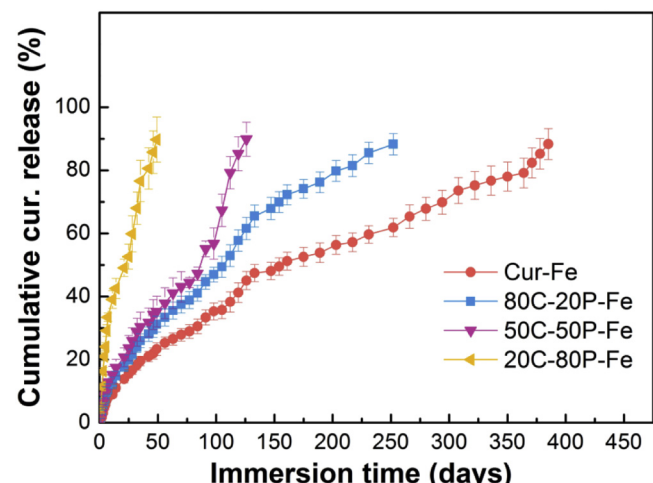
### 3.2. Long-term *in vitro* release kinetics

Fig. 2 shows release profile of curcumin from Cur-Fe and CP-Fe scaffolds. The cumulative releases of the curcumin were determined with respect to the initial incorporated amount of curcumin in the samples as tabulated in Supplemental Table S1. In general, no significant initial burst releases were observed from all the formulations. Based on the release profile, the release rates as indicated by the slopes of the release curves, were increased in the order of Cur-Fe < 80C-20P-Fe < 50C-50P-Fe < 20C-80P-Fe. Therefore, the amount of curcumin in the CP-Fe scaffolds influenced its release kinetic whereby relatively lower release rates of curcumin were observed for scaffolds with higher curcumin amount. With the increase of PLGA composition in CP-Fe scaffolds, faster curcumin releases were observed. The intermolecular interactions between curcumin and PLGA led to the higher curcumin dissolution and consequently increasing the release rate. A part from that,

higher PLGA composition accelerated iron substrate degradation further and this could also trigger curcumin release from the scaffolds as well.

### 3.3. Degradation behaviour

Fig. 3(a) exhibits the potentiodynamic polarization (PDP) curves of pure Fe, Cur-Fe, 80C-20P-Fe, 50C-50P-Fe and 20C-80P-Fe samples. As shown in the figure, the corrosion current densities increased in the order of Cur-Fe < Fe < 80C-20P-Fe < 50C-50P-Fe < 20C-80P-Fe. The



**Fig. 2.** Release kinetics of the curcumin from Cur-Fe, 80C-20P-Fe, 50C-50P-Fe and 20C-80P-Fe samples.

current density is directly proportional to the degradation rate of the scaffolds. **Table 1** shows the corrosion potentials and the degradation rates of Fe, Cur-Fe and CP-Fe scaffolds. Cur-Fe had the lowest degradation rate of 0.10 mm/year and it has been postulated by previous studies that curcumin tended to form a protective layer when adsorbed on metal surfaces and this caused curcumin to slow down the degradation of Fe in the present study [46]. Pure Fe samples gave a degradation rate of 0.23 mm/year while 80C-20P-Fe scaffolds possessed a relatively higher degradation rate of 0.37 mm/year. Further increases in the degradation rate have been shown by 50C-50P-Fe (0.59 mm/year) and 20C-80P-Fe (0.98 mm/year) scaffolds that contained 50 wt% and 80 wt% of added PLGA, respectively. The increase in degradation rates of CP-Fe scaffolds (80C-20P-Fe, 50C-50P-Fe, 20C-80P-Fe) compared to that of pure Fe was attributable to the local acidic hydrolysis of PLGA that had taken place in the scaffolds [30,47]. Higher degradation rate shown by the CP-Fe scaffolds was a favorable outcome in the present study since slow degradation rate of Fe has been a major concern over its use as a temporary implant. Thus, the degradation rate of the Fe scaffolds could be further escalated and controlled by modulating the curcumin-PLGA composition in the CP coating.

**Fig. 3(b)** shows the absolute impedance values of pure Fe, Cur-Fe and 80C-20P-Fe scaffolds at different immersion periods of 7, 14, 21 and 28 days. From day 7 towards day 28 of immersion, the absolute impedance  $|Z|$  of Cur-Fe samples increased from 3743.78  $\Omega$  to 8014.56  $\Omega$  while pure Fe samples also signified an increment of impedance from 3702.10  $\Omega$  at day 7 to 6120.91  $\Omega$  at day 28 and these could be due to the deposition of passive degradation layer that resided on the Fe surface [20]. Meanwhile, with the incorporation of 20 wt% PLGA in 80C-

**Table 1**  
Corrosion potentials and degradation rates of the scaffolds obtained from the PDP test.

Samples	Corrosion potential (mV)	Degradation rate (mm/year)
Cur-Fe	-549.82	0.10 $\pm$ 0.002
Fe	-636.49	0.23 $\pm$ 0.022
80C-20P-Fe	-680.77	0.37 $\pm$ 0.058
50C-50P-Fe	-722.61	0.59 $\pm$ 0.035
20C-80P-Fe	-800.10	0.98 $\pm$ 0.039

20P-Fe samples, the  $|Z|$  value showed a decreasing trend as it decreased from 3400.00  $\Omega$  at day 7 to 2175.34  $\Omega$  at day 28. The acidic hydrolysis of PLGA tended to form pores within PLGA itself leading to the easier electrolyte penetration through the CP coating and subsequently accelerated more degradations on the Fe surface [2,47].

**Fig. 3(c)** shows the weight losses of pure Fe, Cur-Fe, 80C-20P-Fe and PLGA-Fe samples after 7, 14, 21 and 28 days of immersion in PBS solution. From the results, PLGA-Fe samples showed the highest weight loss of 18.9% followed by 80C-20P-Fe (12.05%), pure Fe (7.62%) and Cur-Fe (5.43%) samples after 28 days of immersion. Relatively higher weight loss shown by the 80C-20P-Fe and PLGA-Fe samples could be attributable to the acidic hydrolysis of PLGA that could promote Fe dissolution further. Meanwhile, Cur-Fe samples possessed the lowest weight loss after 28 days immersion and this finding is consistent with previous PDP results that showed the Cur-Fe had the lowest degradation rate.

The pH of the PBS media at different times of immersion for pure Fe, Cur-Fe, 80C-20P-Fe and PLGA-Fe samples is depicted in **Fig. 3(d)**. From the results, the pH of pure Fe changed from 7.4 at day 1 to 10.9 at day

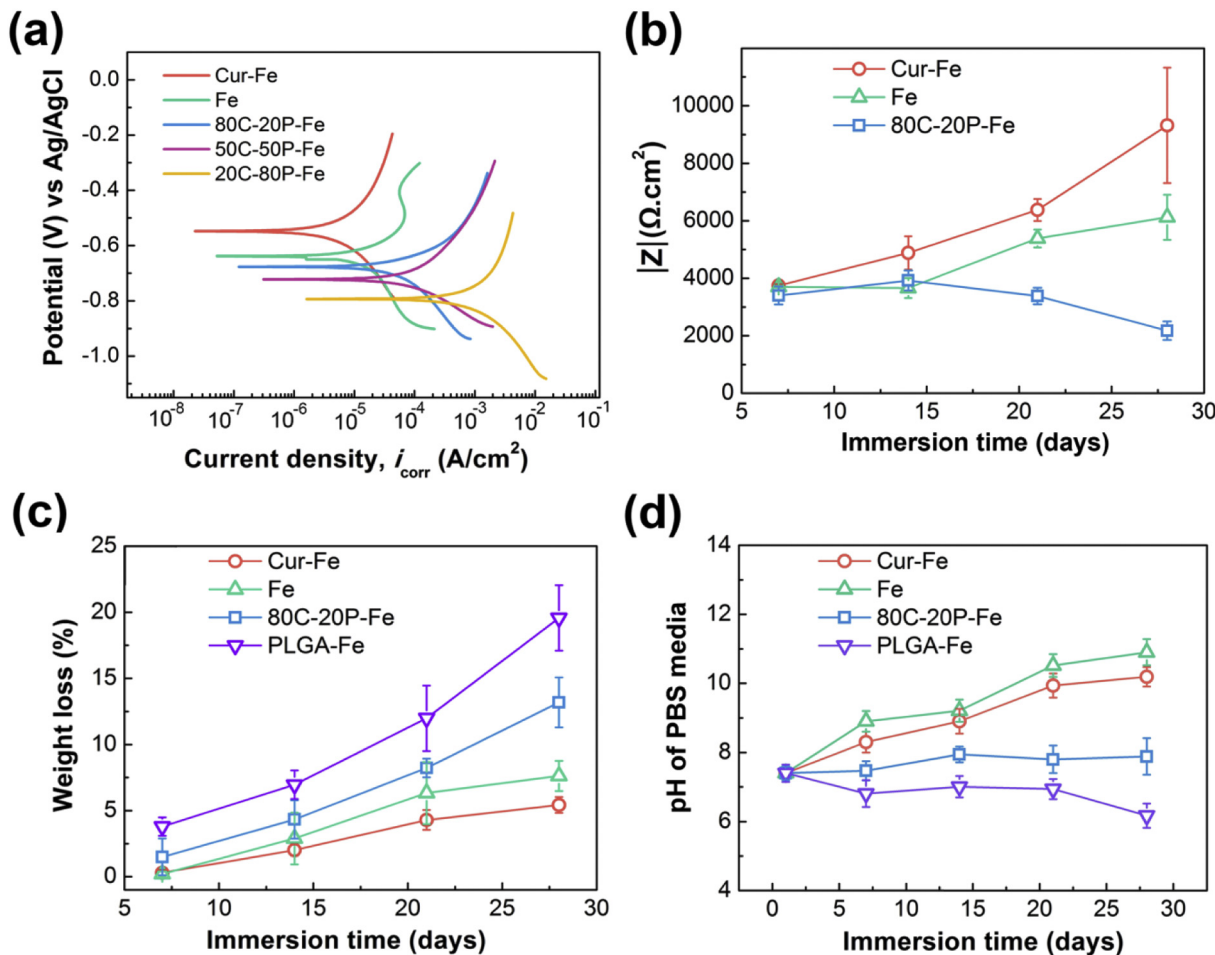


**Fig. 3.** (a) PDP curves of the tested samples, (b) absolute impedance values of the tested samples after 7, 14, 21 and 28 days of immersion, (c) weight losses of the tested samples after 7, 14, 21 and 28 days of immersions, and (d) pH changes of PBS media of the tested samples after 7, 14, 21 and 28 days of immersions.

28. Cur-Fe samples also showed an increment trend as the pH changed from 7.4 at day 1 to 10.19 after 28 days of immersion. It has been known that the degradation of the Fe produces basic  $\text{Fe(OH)}_2$  resulting in an increment of pH. Meanwhile, 80C-20P-Fe samples gave a different pH profile whereby its pH experienced a slight increase to 7.8 at day 28. This slight increase of the pH was ascribed to the pH compensation of the basic product of Fe degradation by acidic hydrolysis of PLGA [30]. PLGA-Fe samples showed a notable pH change to acidic pH as the pH decreased to 6.1 at day 28. Thus, by the incorporation of PLGA, the acidic hydrolysis of PLGA that had taken place in the scaffolds reduced the pH and this effect was prominently seen in the case of PLGA-Fe. In overall, the hydrolysis of PLGA that produced acidic monomers could further

promote Fe dissolution and subsequently leading to the significant weight loss of the scaffolds.

Apart from that, the surface morphology of cleaned Fe surfaces of pure Fe, Cur-Fe and 80C-20P-Fe samples after 28 days of immersions in PBS solution are depicted in Fig. 4. There were pits observed on Fe surface of all the tested samples indicating the occurrence of dissolution on the Fe surface over immersion time. More pits were evidently seen on clean Fe surface of 80C-20P-Fe samples (Fig. 4(a)) signifying relatively more pronounced Fe degradation in the samples compared to those of pure Fe (Fig. 4(c)) and Cur-Fe samples (Fig. 4(e)). In order to identify the oxide degradation products on the cleaned iron surface, the elemental compositions of the cleaned iron surfaces were quantified

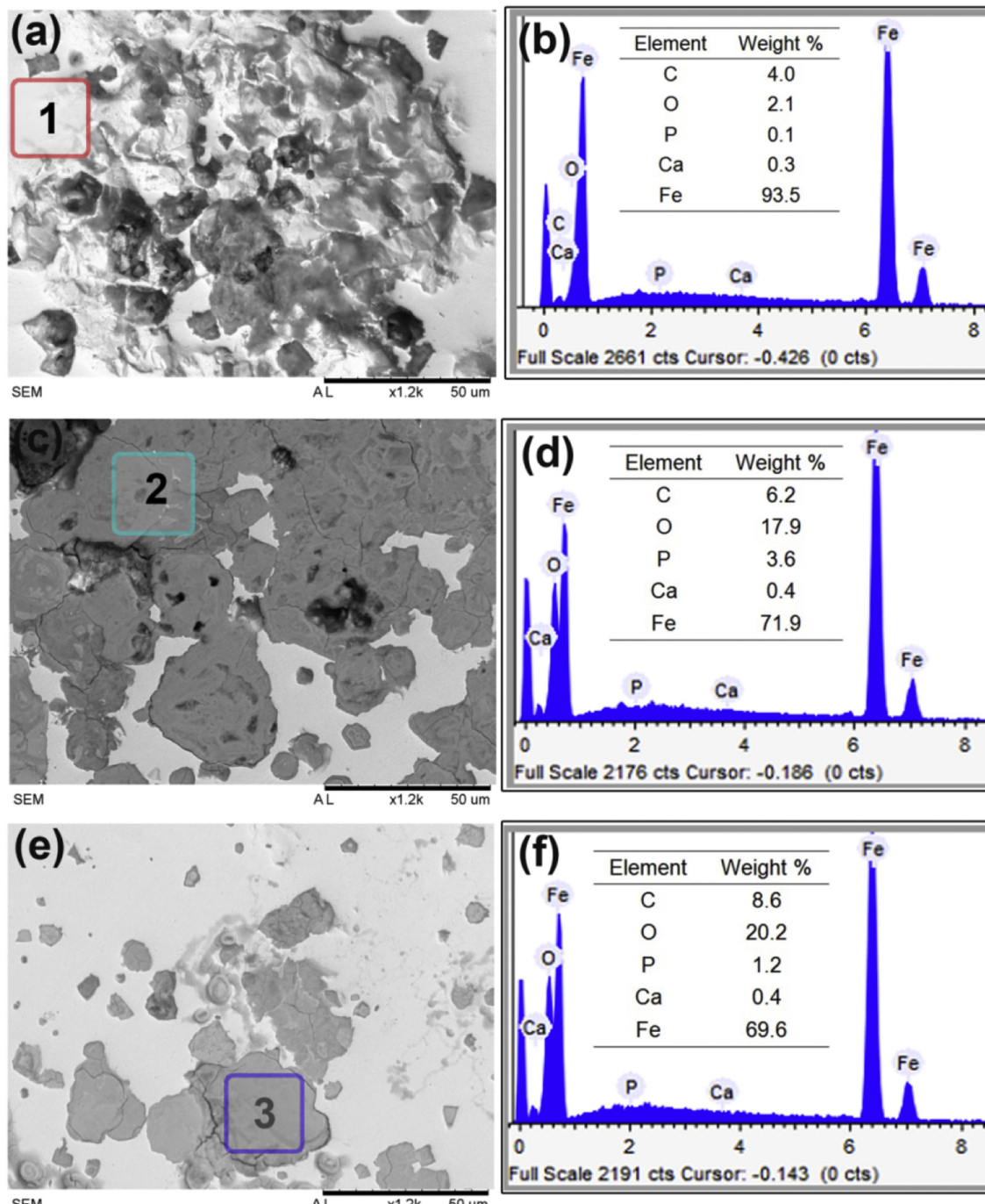


**Fig. 4.** Surface morphology of cleaned Fe surfaces of (a) 80C-20P-Fe, (c) pure Fe, and (e) Cur-Fe samples after 28 days of immersion in PBS solution.

by a simple EDS measurement. The elemental compositions at the selected area on the iron surface were presented in Fig. 4(b,d,f). The area 1 (Fig. 4(b)) with white-coloured phases represent fresh and less-corroded iron surfaces having a relatively low composition of oxygen while area 2 and area 3 with grey-coloured and darker phases correspond to the oxide degradation products of iron as indicated by a higher composition of oxygen (Fig. 4(d,f)).

In bone scaffold applications, an accelerated degradation rate of iron-based scaffolds is highly desirable so that the biodegradation of the scaffolds match with the tissue-healing period. In the present study, Cur-Fe samples with the highest curcumin loading showed a lower degradation rate which in turn, limits its use as a potential bone scaffolds. Nonetheless, the incorporation of PLGA enhanced the degradation of the scaffolds. In bone healing process, the progressive degradation of a scaffold should proceed for 12 to 24 weeks. Thus, the CP-Fe scaffolds (80C-20P-Fe, 50C-50P-Fe, and 20C-80P-Fe) with accelerated degradation rates provided a highly potent alternative to serve as a bone scaffold that fully degraded when the defected bone is completely healed. In order to investigate the biodegradation behaviour of the scaffolds including the optimized degradation rate, a future *in vivo* work could be performed in an animal model to rigorously monitor the degradation functionality of the CP-Fe scaffolds in a more real physiological condition aimed at achieving clinically appropriate degradation rate and optimal bone formation through the scaffolds.

The occurrences of hydrolysis in CP-Fe scaffolds during the course of the immersion were ascertained by evaluating the IR spectra of the dry samples. The PLGA hydrolysis is characterized by an increase in OH peak in IR spectra in the region of  $3200\text{--}3500\text{ cm}^{-1}$  due to the carboxylic acid groups produced through the hydrolysis [30,48,49]. The IR spectra of the dried pure iron, Cur-Fe, 80C-20P-Fe and PLGA-Fe samples taken after 28 days immersion are depicted in Fig. 5. Apparently, the broad and intense peaks at  $3200\text{--}3500\text{ cm}^{-1}$  were clearly observed for both 80C-20P-Fe and PLGA-Fe samples and this compellingly proved the occurrence of hydrolysis of PLGA in those samples. Besides that, the absorbed water on the samples during the IR measurement also could partly contribute to the rise of OH peak in the IR spectra. However, this effect has been minimized by thoroughly drying the samples prior to the ATR-FTIR measurement as stated in the **Materials and methods** part.

The relationship between the degradation of CP-Fe scaffolds and the curcumin release were also analyzed. Fig. 6 depicts the plot of curcumin release rate against the degradation rate of the scaffolds. From the plot, it can be inferred that the curcumin release rate was directly correlated to the degradation rate of the scaffolds. A linear trend has been obtained and this clarified the relationship between the curcumin release and the degradation of the CP-Fe scaffolds. As the iron degradation rate increased in 80C-20P-Fe, 50C-50P-Fe and 20C-80P-Fe scaffolds, the rate of the curcumin release from those scaffolds has escalated as well. The iron substrate degradation would lead to the release of the degradation products from its surface and subsequently triggered the release of the curcumin from the iron substrate. Thus, this correlation signified that the curcumin release kinetics could be controlled by the CP-Fe degradation rate. Among the tested samples, 80C-20P-Fe scaffolds were seen to be the most optimal sample owing to its higher degradation rate as compared to those of pure iron and Cur-Fe samples and to its high curcumin loading. High curcumin loading in the scaffolds is a very crucial parameter to achieve the sustained and extended release of curcumin. Even though 50C-50P-Fe and 20C-80P-Fe scaffolds had a relatively higher degradation rate, as shown in the results, their low curcumin loading limits their potential to provide a sustained curcumin release for an extended time period. From the present study, the acceleration of the iron degradation has been depended on the hydrolysis rate of PLGA. Hence, the selection of appropriate type of PLGA is the key consideration for the long-term effect of the release rate-scaffolds degradation rate dependency. From this aspect, PLGA of a higher LA content and high Mw which possesses slower hydrolysis rate could be

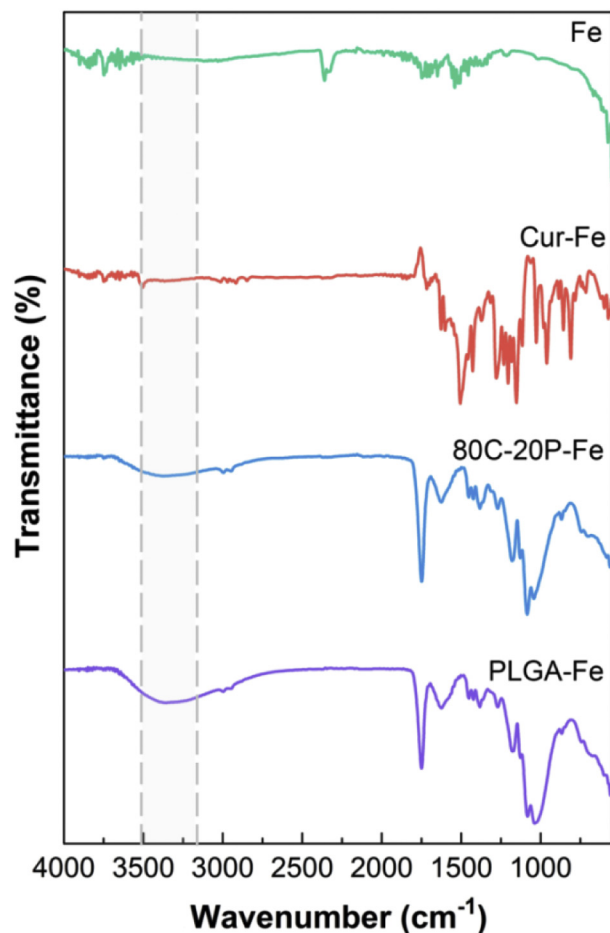


**Fig. 5.** IR spectra of dry pure iron, Cur-Fe, 80C-20P-Fe and PLGA-Fe samples after 28 days of immersion.

an appealing choice to provide continuous degradation acceleration on iron surface and facilitate the slow and sustained curcumin release.

The ionic and electrical conductivity of CP particles were also assessed by means of EIS and four-point probe technique, respectively. From Fig. 7(a), the absolute impedance showed a decreasing trend as the PLGA amount increased. Lower absolute impedance is indicative of improved conductivity of a system. The decrease of the coating impedance as the PLGA composition increased was ascribed to the PLGA's ability to incite ionic conductivity in the CP coating. Polar side chains of carbonyl groups ( $\text{C}=\text{O}$ ) in PLGA could contribute on this ionic

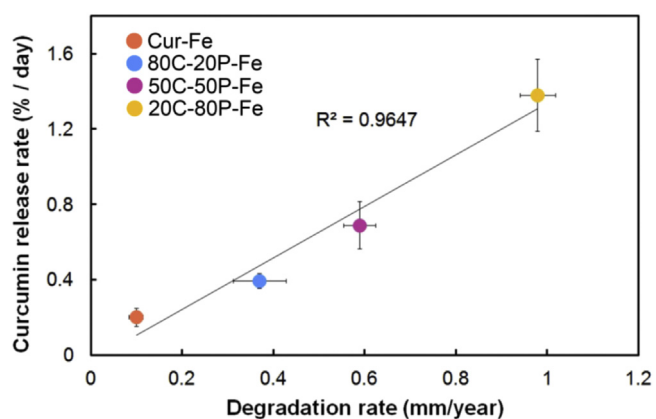


**Fig. 6.** The correlation between the curcumin release rate and the degradation rate of the scaffolds.

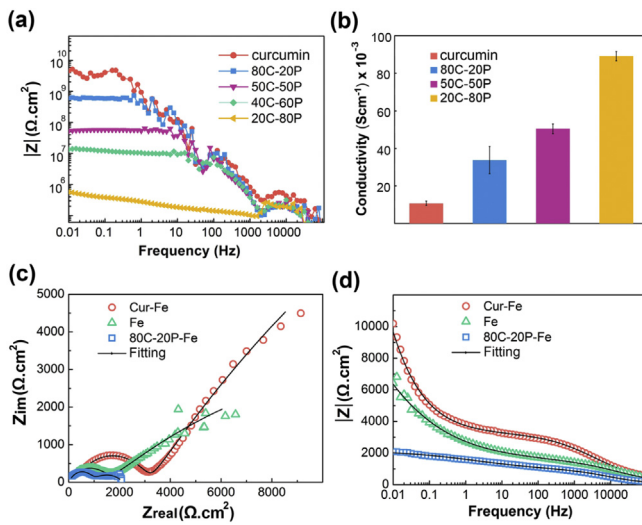


**Fig. 7.** (a) Bode plots (magnitude) of CP samples in PBS solution, (b) electrical conductivity of curcumin and CP particles, (c) fitted Nyquist plots of pure Fe, Cur-Fe and 80C-20P-Fe samples after 28 days of immersion, and (d) fitted Bode plots of pure Fe, Cur-Fe and 80C-20P-Fe samples after 28 days of immersion.

conductivity effect [50]. Besides, the electrical conductivity of CP pellets was also quantified as presented in Fig. 7(b). The conductivity values were determined based the resistance obtained from the I-V curves as shown in Supplemental Fig. S2. The incorporation of PLGA has enhanced the electrical conductivity of the CP whereby the conductivity increased from  $10.77 \times 10^{-3}$  S·cm<sup>-1</sup> for pure curcumin to  $89.16 \times 10^{-3}$  S·cm<sup>-1</sup> for 20C-80P samples. This conductivity enhancement could be attributable to the delocalized electrons in carbonyl C=O groups in PLGA. Thus, the ionic and electrical conductivity effects incited by the PLGA in the CP-Fe scaffolds could assist in enhancing Fe degradation besides its acidic hydrolysis role.

The EIS measurements were performed to further explore the effect of coating and degradation layer on the degradation behaviours of the CP-Fe scaffolds. Fig. 7(c-d) depict the fitted Nyquist plots and Bode plots of pure Fe, Cur-Fe and 80C-20P-Fe samples after 28 days of immersion, respectively. As can be seen from the Nyquist plots, 80C-20P-Fe showed a relatively smaller diameter of the semicircle compared to those of pure Fe and Cur-Fe and this implied its lower charge-transfer resistance,  $R_{ct}$ . The charge-transfer resistance,  $R_{ct}$  represents the resistance of the samples to faradaic charge transfer through degradation and subsequently indicating Fe dissolution [51]. The  $R_{ct}$  value was relatively lower in 80C-20P-Fe samples (808.43 Ω) implying more pronounced Fe degradation as compared to those of pure Fe (1646.0 Ω) and Cur-Fe (2280.33 Ω) samples [52]. Besides, it also connoted a higher susceptibility of electrolyte permeation through the CP coating in the 80C-20P-Fe scaffolds [53]. Bode plot indicates the absolute impedance value of a tested sample. As depicted in Fig. 7(d), after 28 days of immersion, Cur-Fe samples had the impedance value of 9319.33 Ω while pure Fe and 80C-20P-Fe samples gave the impedance values of 6120.91 Ω and 2175.34 Ω, respectively. Thus, it can be inferred here that the 80C-20P-Fe samples had a relatively higher current flow over the immersion times and this was consistent with the findings from the PDP test which indicated that the 80C-20P-Fe samples had relatively higher current density compared to those of pure Fe and Cur-Fe samples.

The fitting of the experimental impedance responses yielded values of the least-squares fit parameter,  $\chi^2$  around  $10^{-3}$  as tabulated in Table 2, indicating that the EIS simulations fitted the experimental data well. Table 2 summarizes the values of charge-transfer resistance  $R_{ct}$  and absolute impedance  $|Z|$  for pure Fe, Cur-Fe and 80C-20P-Fe samples after 28 days of immersion.

A finite-element simulation was performed to compare the degradation of the Cur-Fe and 80C-20P-Fe scaffolds. Fig. 8(a) displays the

**Table 2**

Charge-transfer resistance  $R_{ct}$ , absolute impedance  $|Z|$  and chi-squared values ( $\chi^2$ ) of the fittings for pure Fe, Cur-Fe and 80C-20P-Fe samples.

Samples	Charge-transfer resistance, $R_{ct}$ (Ω)	$ Z (\Omega)$	$\chi^2$ (fitting)
Pure Fe	$1646.00 \pm 124.18$	$6120.91 \pm 785.13$	$4.82 \times 10^{-3}$
Cur-Fe	$2280.33 \pm 628.03$	$9319.33 \pm 2002.9$	$1.43 \times 10^{-3}$
80C-20P-Fe	$808.43 \pm 153.30$	$2175.34 \pm 92.17$	$1.65 \times 10^{-3}$

tetrahedral meshing constructed to run the model of the samples while Fig. 8(b) depicts the two layers representing the iron surface and the CP/curcumin coating layers. Fig. 8(c) and (d) below shows the distribution of the current density on the top surface of Cur-Fe and 80C-20P-Fe scaffolds after immersion in the PBS media, respectively. The corrosion current density on the top surface (coating layer) of 80C-20P-Fe samples was relatively higher than that of Cur-Fe surface and this subsequently promoted a higher degradation rate in the 80C-20P-Fe scaffolds. Higher electrical conductivity of the 80C-20P coating led to this enhanced coating current density. Fig. 8(e) and (f) displays the distribution of the current density on the iron surface of Cur-Fe and 80C-20P-Fe scaffolds after immersion in the PBS media, respectively. Apparently, a higher current flow has been observed on the iron surface of 80C-20P-Fe scaffolds in comparison to that of Cur-Fe and this finding was consistent with previous polarization test and weight loss results showing relatively more pronounced degradation in the 80C-20P-Fe scaffolds. The hydrolysis of 20 wt% PLGA incorporated in the 80C-20P-Fe scaffolds facilitated the electrolyte ingress into iron surface and thus subsequently promoted more redox reactions taken place on the iron surface.

#### 3.4. Interfacial interactions by XPS and ATR-FTIR

Fig. 9(a) shows the survey spectra showing the elements existed in the of 80C-20P-Fe samples. It is evidently seen that oxygen (O), carbon (C) and iron (Fe) constituted the 80C-20P-Fe samples. Fig. 9(b) shows the high-resolution spectra of C1s for 80C-20P-Fe samples. The peak at 284.79 eV represents the C—C/C=C/C—H of the curcumin and PLGA while peaks at 286.13, 287.34 and 288.37 eV represent C—OH, C—O—C (aromatic) and C—O—C (aliphatic) of curcumin and PLGA [54]. Binding energy at 289.23 eV corresponds to the C=O in PLGA and curcumin molecules [55]. The peak at 290.05 eV is ascribed to the carbon in carboxylate O=C—O— group of hydrolyzed PLGA [56]. The peak at 291.12 eV is attributable to the carbon in undissociated carboxylic acid groups (O=C—OH) in PLGA [57,58].

Fig. 9(c) shows the high-resolution spectra of O1s for 80C-20P-Fe samples. The peaks at 529.3 and 530.8 eV correspond to oxides (O<sup>2-</sup>) and carboxylates COO<sup>-</sup> from PLGA, respectively [59]. The peak at 531.8 eV represents the C=O species in PLGA and curcumin while the peak at 532.14 eV is attributable to the C—O—C from PLGA (aliphatic). The peak appearing at 532.40 eV was contributed by C—O—C species from curcumin (aromatic) while the peak at 533.17 eV representing C—OH species in curcumin [60]. Peaks at 533.85 eV (O<sup>2-</sup>=C—OH) and 535.5 eV (O=C—O<sup>2-</sup>H) represent the oxygen atoms of undissociated carboxylic acid groups in PLGA [59]. Based on the high-resolution spectra of C1s of 80C-20P-Fe samples, C=O peaks have shifted to higher binding energy from 288.32 eV (binding energy of C=O of pure PLGA, as presented in Supplemental Fig. S3) to 289.43 eV. Higher electron withdrawing capacity of iron removed more valence electrons of carbon atom in the carbonyl group, leading to the enhancement of effective nuclear charge experienced by the core-electron and subsequently increasing the electron binding energy [30].

Fig. 9(d) shows the IR spectra of PLGA's carbonyl (C=O) groups in the tested CP-Fe scaffolds. As can be seen from the figure, C=O peaks of CP-Fe samples (80C-20P-Fe, 50C-50P-Fe, 20C-80P-Fe) shifted to higher wavenumber with respect to that of pure PLGA. In addition, the curcumin's C=O peak in the CP-Fe scaffolds (80C-20P-Fe) was also

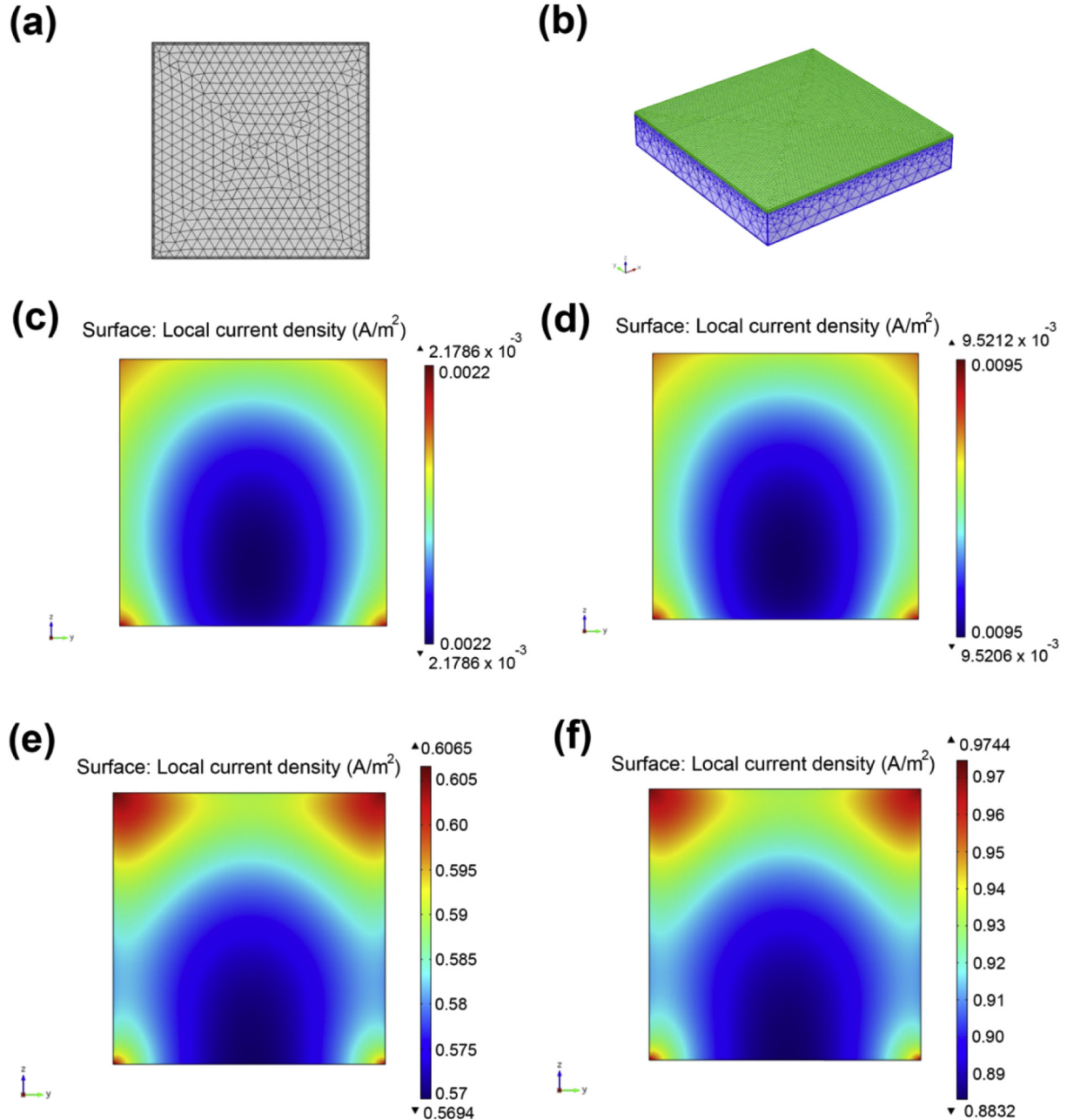


**Fig. 8.** (a) The tetrahedral mesh of the modeling, (b) the 3-D modeling of coated Fe surface, and the local current density of the (c,e) Cur-Fe and (d,f) 80C-20P-Fe scaffolds after immersion in PBS media.

shifted as depicted in Fig. 9(e). These shiftings suggest that the carbonyl groups in CP coating could be interconnected via intermolecular hydrogen bonding and once deposited on Fe surface, the bonding was disrupted and consequently causing the C=O peaks to be shifted upwards [61]. Thus, the shiftings of the carbonyl C=O peaks in both XPS and ATR-FTIR measurements evidently showed that there were interfacial interactions between the CP coating and Fe surface. The interfacial interactions between CP and Fe surface could assist in enhancing mechanical strengths of the scaffolds.

### 3.5. Mechanical properties

Fig. 10(a) shows the stress-strain curves of the scaffolds under uniaxial compressive load and the inset displaying the enlargement of the elastic deformation region. From the figure, it can be seen that the

incorporation of curcumin and PLGA into porous Fe structure have escalated CP-Fe scaffolds' mechanical strengths. The compressive strengths and stiffness increased with the increasing amount of the PLGA as shown in Table S2 (Supplementary information). Fig. 10(b) shows the slope values of AFM's retraction curves which are directly proportional to the stiffness of the measured particles. Based on the result, 20C-80P particles with 80 wt% PLGA showed a relatively higher slope of 12.31 N/m as compared to those of 80C-20P particles (5.87 N/m) and pure curcumin particles (2.41 N/m). The higher slope values, in other words, the enhancement of the stiffness shown by CP particles as compared to that of pure curcumin particles have led to the difference of strengths between Cur-Fe and CP-Fe scaffolds. Thus, the stiffness of the CP-Fe particles substantially enhanced CP-Fe's mechanical strengths besides the interfacial interactions developed between the CP coating and the Fe surface.

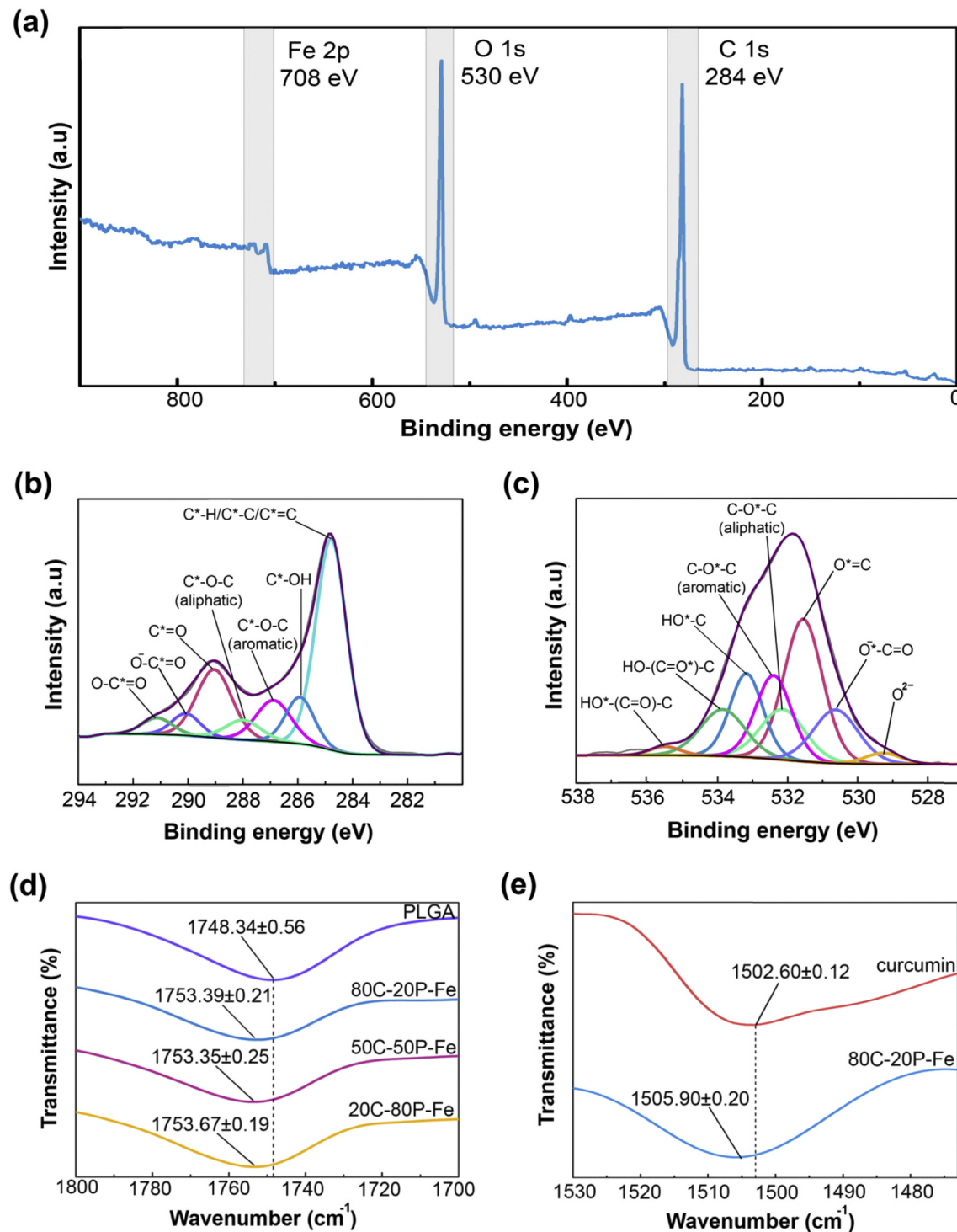


**Fig. 9.** (a) Survey spectra of 80C-20P-Fe samples, (b) C1s peak deconvolution of 80C-20P-Fe scaffolds, (c) O1s peak deconvolution of 80C-20P-Fe scaffolds, (d) shifting of the IR spectra of PLGA's carbonyl (C=O) groups in CP-Fe scaffolds, and (e) shifting of the IR spectra of curcumin's carbonyl (C=O) groups in 80C-20P-Fe scaffolds.

### 3.5.1. Mechanical-degradation relationship

In the present study, the compressive strengths and the stiffness of all the CP-Fe scaffolds are within the range of the cancellous bone's compressive strength (0.1–16 MPa) and stiffness (10–1570 MPa) [62,63]. This within-the-range strength is a vital characteristic of an ideal bone scaffold. An ideal biodegradable scaffold should provide adequate temporary mechanical support while maintaining its progressive degradation [7]. In bone healing process, the mechanical support provided by bone scaffolds should be sustained for 12–24 weeks (3–6 months) [64]. The mechanical properties of Cur-Fe, 80C-20P-Fe and 50C-50P-Fe

scaffolds after 28 days of immersion were determined to assess the effect of degradation on the mechanical integrity of the scaffolds. Fig. 10 (c–d) shows the compressive strengths and stiffness of Cur-Fe, 80C-20P-Fe and 50C-50P-Fe scaffolds before and after 28 days of immersion. After 28 days of immersion, the compressive strengths of the 80C-20P-Fe and 50C-50P-Fe scaffolds have reduced by 9–14% with the increase of PLGA composition as shown in Fig. 10(c). This trend was attributable to the relatively higher degradation rate of 80C-20P-Fe and 50C-50P-Fe scaffolds as compared to that of Cur-Fe. A part from that, the stiffness of the samples also showed a decrement trend with the progress of

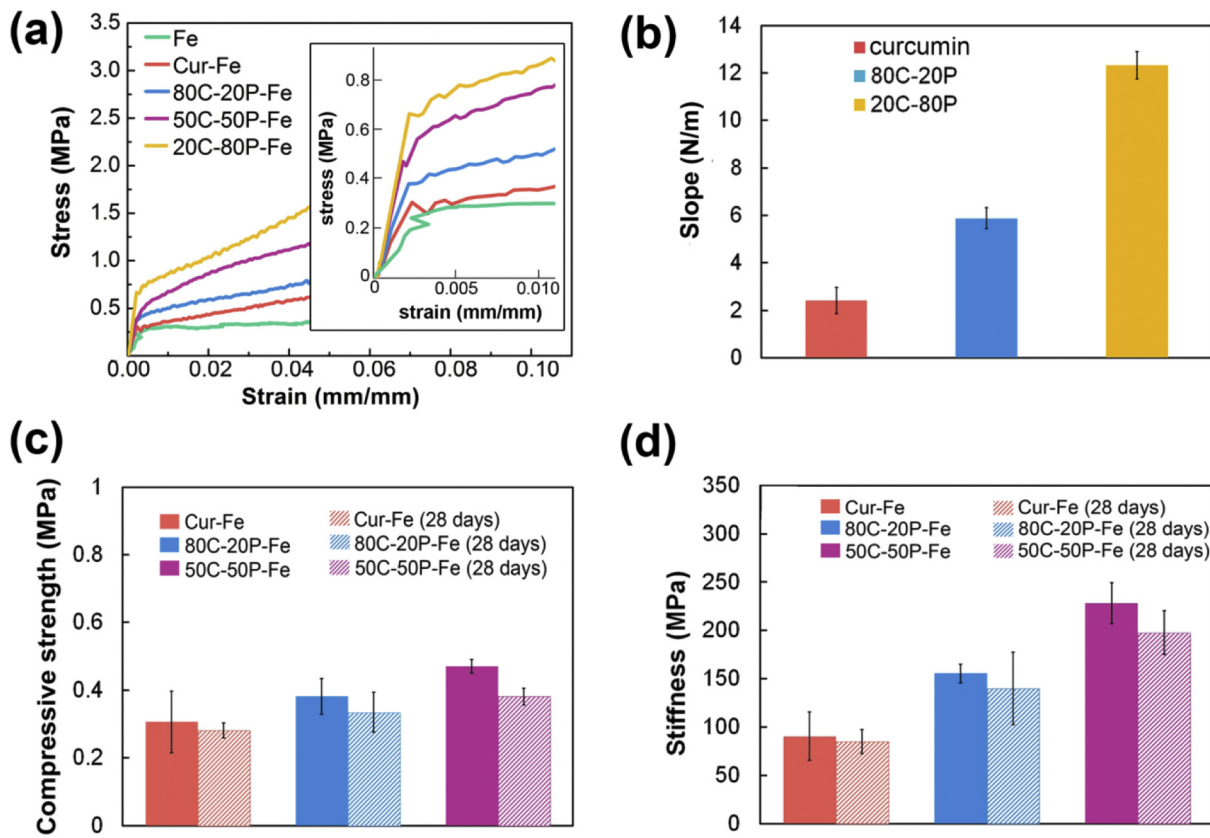


**Fig. 10.** (a) Stress-strain curves of the samples, and inset shows the enlargement of elastic deformation region, (b) slope values of AFM retraction curves for curcumin, 80C-20P particles and 20C-80P particles, (c) compressive strengths and (d) stiffness of Cur-Fe, 80C-20P-Fe and 50C-50P-Fe scaffolds before and after 28-days immersion.

immersion time. Thus, from the results, it is inferred that the degradation of the scaffolds has influenced the mechanical integrity of the CP-Fe scaffolds throughout the immersion period. Nevertheless, based on the decrement value, the degradations of CP-Fe scaffolds have not abruptly ruptured scaffolds' mechanical strengths as an appropriate strengths reduction has been attained. Thus, it is expected that the CP-Fe scaffolds could meet the time frame of bone healing time to provide adequate mechanical support.

### 3.6. Cell viability test

Fig. 11 shows the viability of the osteosarcoma (OS) MG-63 cells after 7, 14, 21 and 28 days incubation with the 80C-20P-Fe and Cur-Fe scaffolds. From the figure, it was evidently seen that Cur-Fe and 80C-20P-Fe samples significantly arrested the growth of osteosarcoma (OS) cells. Pure Fe did not retard the OS cells growth with the progression of time except on day 7 of incubation. However, as time progresses (i.e. 14 to 28 days), no significant cells arrest observed for the pure Fe samples and this occurrence could be ascribed to the cellular adaptations of the OS cells which is in-line with other studies of Fe-based scaffolds, which showed a higher cell viability and no growth inhibition as the culture-time progresses [65,66]. Meanwhile, the OS cell viability of pure PLGA samples did not change much as the OS cell viability remained >85% over the course of incubation time. This indicated that the acidic hydrolysis products of PLGA did not pose significant growth-arresting effect on the OS cells. Since pure PLGA and pure Fe samples have not shown significant effect on OS cell arrest, the ability of Cur-Fe and 80C-20P-Fe samples to retard the OS cell growths was mainly attributed to the presence of curcumin owing to its ability to induce cell cycle arrest and apoptosis in the OS cell line [67]. Nevertheless, the insignificant growth-arresting effects shown by PLGA hydrolysis and Fe substrate degradation could be advantageous in such a way

that they could not negate the growth of normal healthy cells during the bone formation process.

Iron-based material has been vastly studied for biomedical applications. It has a great potential as biodegradable bone scaffolds [27], coronary stents [68] and nanoparticles [69]. A recent long-term animal study performed by [70] demonstrated that after 53-month implantation, severe degradation has been observed on the nitrided iron scaffold with a large amount of insoluble corrosion products. However, there was only slight inflammation without tissue necrosis, hypersensitivity or any other abnormalities found after the implantation in the porcine model. This indicated that the insoluble Fe degradation products could impose

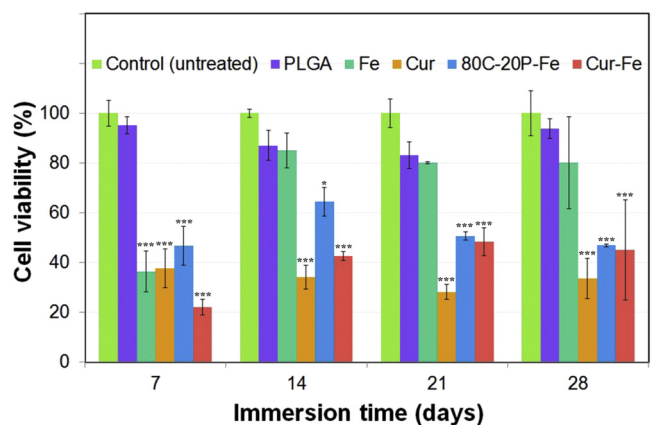


**Fig. 11.** Cell viabilities of the Cur-Fe and 80C-20P-Fe scaffolds after 7, 14, 21, 28 of incubation days. (\*\* represents significant difference of  $p < 0.01$ , and \* represents  $p < 0.05$ ,  $n = 3$ ). The data were analyzed by comparison of untreated cells (control) to treatment groups at each time point by using 1-way ANOVA with Tukey's multiple comparisons tests at triplicates.

a good long-term biocompatibility to the local tissues. Nevertheless, the excessive release of Fe ions and low bioresorption of Fe insoluble degradation particles such as  $\text{Fe}_3\text{O}_4$ ,  $\text{Fe}_2\text{O}_3$  and  $\text{Fe}(\text{OH})_3$  could lead to a decline in cytocompatibility and tissue regenerations due to the possible induced toxicity. Some studies also reported a poor biocompatibility of Fe-based scaffold particularly in *in vitro* condition due to the accumulations of insoluble iron oxides and excessive release of Fe ions [26,71]. In this regard, an appropriate control on its degradation rate and subsequent ions release is necessary so as to make sure the ions concentration is within the tolerable limit.

The cells viability study can be extended to the normal healthy cells of bone to evaluate the effect of CP-Fe degradation on surrounding healthy tissues. *In vivo* mechanical-degradation tailoring study could also be performed to monitor the degradation functionality of the CP-Fe scaffolds aimed at achieving clinically appropriate degradation and optimal bone formation through the scaffolds without compromising the temporary mechanical function. These studies are all part of the future work planned in this system.

### 3.7. Proposed structure-function relationships in CP-Fe scaffolds

An understanding on the structure-function relationships of the constituted materials is essential in the design of effective drug-device systems. In the present study, the proposed structure-function relationships in CP-Fe scaffolds has been addressed based

on the interactions between PLGA, curcumin, and Fe, thus establishing a relationship between compositions, structure, observed properties and functionalities. The functionalities of the CP-Fe scaffolds have been improved by the incorporation of PLGA in terms of curcumin-release kinetics, scaffold degradation and mechanical properties. Fig. 12 depicts the schematic diagram illustrating the effects of the structure-function relationships of PLGA, curcumin, and Fe on CP-Fe's degradation and curcumin release. In the release test, intermolecular interactions between PLGA and curcumin as well as the degradation of the porous Fe substrate influenced the curcumin release kinetics. Furthermore, since the bone formation is a long-term process, the slow and sustained releases of curcumin from Cur-Fe and 80C-20P-Fe scaffolds are beneficial and have a significant effect on the OS cell arrest in the present study. In scaffold degradation aspect, the hydrolysis of PLGA producing soluble monomers of lactic acid and glycolic acid could activate micropores within itself and this facilitated electrolyte ingress towards the Fe surface and thus escalating the Fe degradation rate further. The degradation of Fe substrate also facilitated the curcumin release as there was a direct correlation between the scaffolds degradation rates and curcumin release rate. The stiffness of the CP particles mainly depended on PLGA-curcumin composition and has led to the enhanced mechanical strengths of the CP-Fe scaffolds. The degradations of CP-Fe scaffolds have not abruptly ruptured their mechanical strengths as an appropriate strength reduction (9–14%)

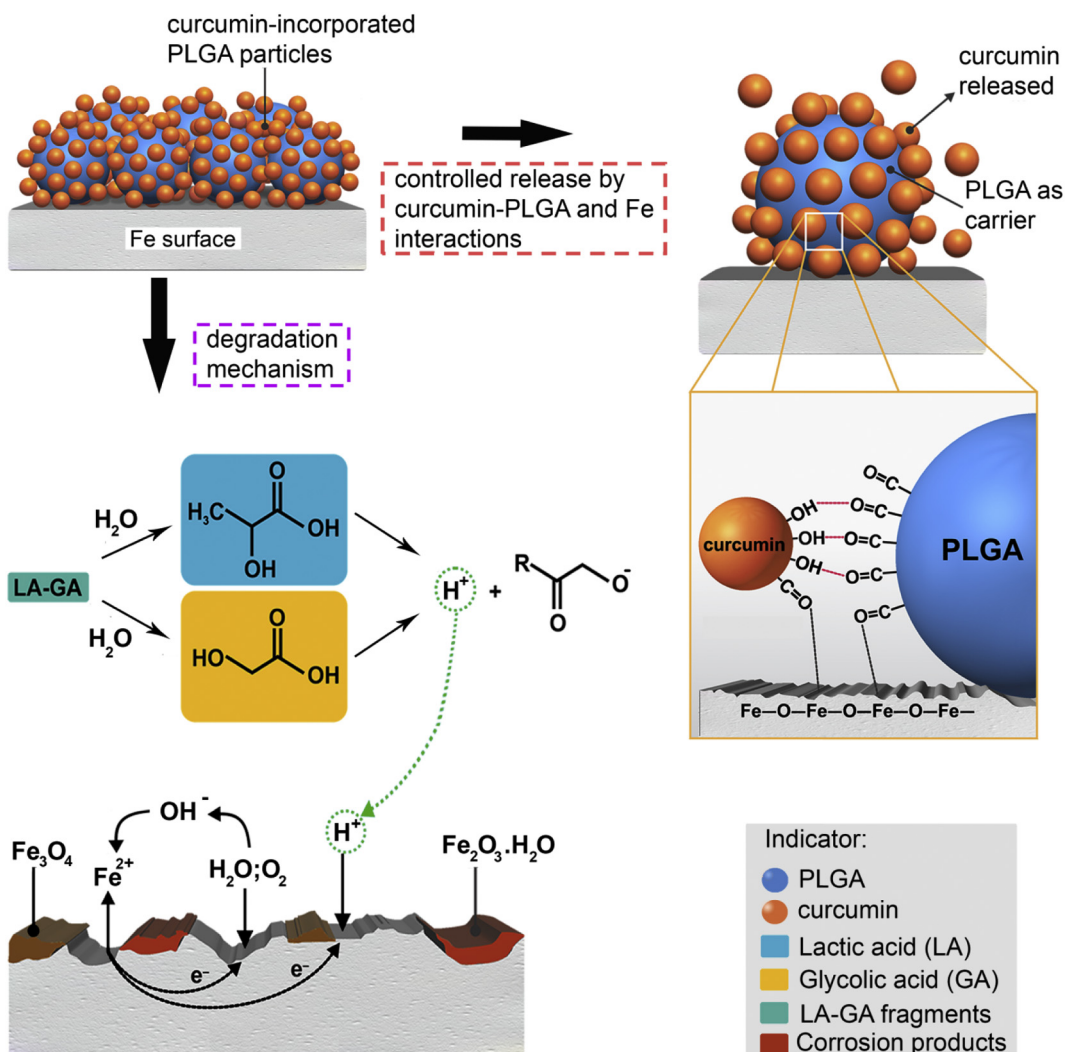


Fig. 12. Schematic diagram illustrating the effect of structure-function relationship between PLGA, curcumin and Fe on CP-Fe's degradation and curcumin release.

has been attained after 28 days of immersion. In overall, the effects of PLGA incorporation were prominently observed in the curcumin release kinetics, CP-Fe degradation, scaffolds mechanical strengths and the interfacial interactions between the CP coating and Fe surface.

## 4. Conclusion

In the present study, PLGA's hydrolysis and its ionic conductivity promoted CP-Fe's degradation further. The degradation of iron substrate could drive the release kinetics of the curcumin. In the mechanical aspect, the stiffness of the CP particles and the interfacial interactions developed between CP coating and Fe surface has further enhanced CP-Fe's mechanical strengths. The scaffolds showed an appropriate strengths reduction after 28 days of immersion. The CP-Fe scaffolds showed its high potential as a bone cancer scaffold by significantly retarding the growth of the osteosarcoma cells owing to the cancer-arresting effect of curcumin. The PLGA hydrolysis and the degradation of Fe substrate posed no prominent effect on the arrest of the osteosarcoma cells growth. In overall, this study demonstrated that the PLGA has played vital roles in this drug-device system in controlling curcumin release, expediting and tailoring Fe degradation and assisting in the enhancement of scaffolds' mechanical strength.

## Acknowledgement

The authors gratefully acknowledge the Malaysian Ministry of Education and Universiti Teknologi Malaysia under the Long Term Research Grant Scheme (R.K130000.734004L825) and Natural Sciences and Engineering Research Council of Canada (NSERC). The authors thank Mr. Kim Bumsoo, Alantum Korea for providing the porous iron sheets.

## Authors' contribution

A.H.M., H.N. and H.H. designed the study. A.H.M. developed all the studies under the supervision of H.H., H.N. and M.R.A.K. M.N.S. developed the cell viability study under the supervision of Q.U.H. A.H.M. wrote the manuscript with the input from all other authors, including F.S.J. and D.H. H.N. approved the manuscript.

## Appendix A. Supplementary data

Supplementary data to this article can be found online at <https://doi.org/10.1016/j.matdes.2018.09.019>.

## References

- [1] K. Kruckiewicz, J.K. Zak, Biomaterial-based regional chemotherapy: local anticancer drug delivery to enhance chemotherapy and minimize its side-effects, *Mater. Sci. Eng. C* 62 (2016) 927–942.
- [2] Y. Shi, J. Pei, L. Zhang, B.K. Lee, Y. Yun, J. Zhang, Z. Li, S. Gu, K. Park, G. Yuan, Understanding the effect of magnesium degradation on drug release and anti-proliferation on smooth muscle cells for magnesium-based drug eluting stents, *Corros. Sci.* 123 (2017) 297–309.
- [3] H. Ma, T. Li, Z. Huan, M. Zhang, Z. Yang, J. Wang, J. Chang, C. Wu, 3D printing of high-strength bioscaffolds for the synergistic treatment of bone cancer, *NPG Asia Mater.* 10 (2018) 31–44.
- [4] A.H. Yusop, A.A. Bakir, N.A. Shaharom, M.R. Abdul Kadir, H. Hermawan, Porous biodegradable metals for hard tissue scaffolds: a review, *Int. J. Biomater.* 2012 (2012), 641430.
- [5] J.O. Gordeladze, H.J. Haugen, S.P. Lyngstadaas, J.E. Reseland, Bone tissue engineering: state of the art, challenges, and prospects, in: A. Hasan (Ed.), *Tissue Engineering for Artificial Organs*, Wiley-VCH, New Jersey 2017, pp. 525–548.
- [6] M. Yazdimamaghani, M. Razavi, D. Vashaei, K. Moharamzadeh, A.R. Boccaccini, L. Tayebi, Porous magnesium-based scaffolds for tissue engineering, *Mater. Sci. Eng. C* 71 (2017) 1253–1266.
- [7] H. Hermawan, Updates on the research and development of absorbable metals for biomedical applications, *Prog. Biomater.* 7 (2) (2018) 93–110.
- [8] X. Wang, S. Xu, S. Zhou, W. Xu, M. Leary, P. Choong, M. Qian, M. Brandt, Y.M. Xie, Topological design and additive manufacturing of porous metals for bone scaffolds and orthopaedic implants: a review, *Biomaterials* 83 (2016) 127–141.
- [9] D. Hong, D.-T. Chou, O.I. Velikokhatnyi, A. Roy, B. Lee, I. Swink, I. Issaev, H.A. Kuhn, P.N. Kumta, Binder-jetting 3D printing and alloy development of new biodegradable Fe-Mn-Ca/Mg alloys, *Acta Biomater.* 45 (2016) 375–386.
- [10] H.M. Wong, P.K. Chu, F.K.L. Leung, K.M.C. Cheung, K.D.K. Luk, K.W.K. Yeung, Engineered polycaprolactone-magnesium hybrid biodegradable porous scaffold for bone tissue engineering, *Prog. Nat. Sci.* 24 (5) (2014) 561–567.
- [11] A. Brown, S. Zaky, H. Ray, C. Sfeir, Porous magnesium/PLGA composite scaffolds for enhanced bone regeneration following tooth extraction, *Acta Biomater.* 11 (2015) 543–553.
- [12] M.Q. Cheng, T. Wahafu, G.F. Jiang, W. Liu, Y.Q. Qiao, X.C. Peng, T. Cheng, X.L. Zhang, G. He, X.Y. Liu, A novel open-porous magnesium scaffold with controllable microstructures and properties for bone regeneration, *Sci. Rep.* 6 (2016) 24134.
- [13] M. Yazdimamaghani, M. Razavi, D. Vashaei, L. Tayebi, Surface modification of biodegradable porous Mg bone scaffold using polycaprolactone/bioactive glass composite, *Mater. Sci. Eng. C* 49 (2015) 436–444.
- [14] E. Aghion, Y. Perez, Effects of porosity on corrosion resistance of Mg alloy foam produced by powder metallurgy technology, *Mater. Charact.* 96 (2014) 78–83.
- [15] L. Zhao, Z. Zhang, Y. Song, S. Liu, Y. Qi, X. Wang, Q. Wang, C. Cui, Mechanical properties and in vitro biodegradation of newly developed porous Zn scaffolds for biomedical applications, *Mater. Des.* 108 (2016) 136–144.
- [16] R. Alavi, A. Trenggono, S. Champagne, H. Hermawan, Investigation on mechanical behavior of biodegradable iron foams under different compression test conditions, *Metals* 7 (6) (2017) 202.
- [17] C. Yang, Z. Huan, X. Wang, C. Wu, J. Chang, 3D printed Fe scaffolds with HA nanocoating for bone regeneration, *ACS Biomater. Sci. Eng.* 4 (2) (2018) 608–616.
- [18] J. Čapek, Š. Msallamová, E. Jablonská, J. Lipov, D. Vojtěch, A novel high-strength and highly corrosive biodegradable Fe-Pd alloy: structural, mechanical and in vitro corrosion and cytotoxicity study, *Mater. Sci. Eng. C* 79 (2017) 550–562.
- [19] R. Oriňáková, A. Oriňák, M. Giretová, L. Medvecký, M. Kupková, M. Hrubovčáková, I. Maskalová, J. Macko, F. Kalavský, A study of cytocompatibility and degradation of iron-based biodegradable materials, *J. Biomater. Appl.* 30 (7) (2016) 1060–1070.
- [20] T. Kraus, F. Moszner, S. Fischerauer, M. Fiedler, E. Martinelli, J. Eichler, F. Witte, E. Willbold, M. Schinhammer, M. Meischel, P.J. Uggowitzer, J.F. Löffler, A. Weinberg, Biodegradable Fe-based alloys for use in osteosynthesis: outcome of an *in vivo* study after 52 weeks, *Acta Biomater.* 10 (7) (2014) 3346–3353.
- [21] M. Dehestani, E. Adolfsson, L.A. Stanciu, Mechanical properties and corrosion behavior of powder metallurgy iron-hydroxyapatite composites for biodegradable implant applications, *Mater. Des.* 109 (2016) 556–569.
- [22] W.J. Lin, D.Y. Zhang, G. Zhang, H.T. Sun, H.P. Qi, L.P. Chen, Z.Q. Liu, R.L. Gao, W. Zheng, Design and characterization of a novel biocorrodible iron-based drug-eluting coronary scaffold, *Mater. Des.* 91 (2016) 72–79.
- [23] Y.P. Feng, N. Gaztelumendi, J. Fornell, H.Y. Zhang, P. Solsona, M.D. Baró, S. Suriñach, E. Ibáñez, L. Barrios, E. Pellicer, C. Nogués, J. Sort, Mechanical properties, corrosion performance and cell viability studies on newly developed porous Fe-Mn-Si-Pd alloys, *J. Alloys Compd.* 724 (2017) 1046–1056.
- [24] Y. Feng, J. Fornell, H. Zhang, P. Solsona, M.D. Baró, S. Suriñach, E. Pellicer, J. Sort, Synthesis of  $\alpha$ -Fe<sub>2</sub>O<sub>3</sub> and Fe-Mn oxide foams with highly tunable magnetic properties by the replication method from polyurethane templates, *Materials* 11 (2) (2018) 280.
- [25] J. Čapek, D. Vojtěch, A. Oborná, Microstructural and mechanical properties of biodegradable iron foam prepared by powder metallurgy, *Mater. Des.* 83 (2015) 468–482.
- [26] J. He, F.L. He, D.W. Li, Y.L. Liu, D.C. Yin, A novel porous Fe/Fe-W alloy scaffold with a double-layer structured skeleton: preparation, in vitro degradability and biocompatibility, *Colloids Surf. B* 142 (2016) 325–333.
- [27] Y. Su, S. Champagne, A. Trenggono, R. Tolouei, D. Mantovani, H. Hermawan, Development and characterization of silver containing calcium phosphate coatings on pure iron foam intended for bone scaffold applications, *Mater. Des.* 148 (2018) 124–134.
- [28] S. Ray, U. Thormann, M. Eichelroth, M. Budak, C. Biehl, M. Rupp, U. Sommer, T. El Khassawna, F.I. Alagboso, M. Kampschulte, M. Rohnke, A. Henß, K. Peppler, V. Linke, P. Quadbeck, A. Voigt, F. Stenger, D. Karl, R. Schnettler, C. Heiss, K.S. Lips, V. Alt, Strontium and bisphosphonate coated iron foam scaffolds for osteoporotic fracture defect healing, *Biomaterials* 157 (2018) 1–16.
- [29] M. Zamani, M.P. Prabhakaran, J. Varshosaz, P.S. Mhaisalkar, S. Ramakrishna, Electrosprayed Montelukast/poly (lactic-co-glycolic acid) particle based coating: a new therapeutic approach towards the prevention of in-stent restenosis, *Acta Biomater.* 42 (2016) 316–328.
- [30] A.H. Yusop, N.M. Daud, H. Nur, M.R. Kadir, H. Hermawan, Controlling the degradation kinetics of porous iron by poly(lactic-co-glycolic acid) infiltration for use as temporary medical implants, *Sci. Rep.* 5 (2015) 11194.
- [31] R. Chang, L. Sun, T.J. Webster, Selective inhibition of MG-63 osteosarcoma cell proliferation induced by curcumin-loaded self-assembled arginine-rich-RGD nanoparticles, *Int. J. Nanomedicine* 10 (2015) 3351–3365.
- [32] M.M. Yallappu, B.K. Gupta, M. Jaggi, S.C. Chauhan, Fabrication of curcumin encapsulated PLGA nanoparticles for improved therapeutic effects in metastatic cancer cells, *J. Colloid Interface Sci.* 351 (1) (2010) 19–29.
- [33] W. Jiang, L. Li, D. Zhang, S. Huang, Z. Jing, Y. Wu, Z. Zhao, L. Zhao, S. Zhou, Incorporation of aligned PCL-PEG nanofibers into porous chitosan scaffolds improved the orientation of collagen fibers in regenerated periodontium, *Acta Biomater.* 25 (2015) 240–252.
- [34] D.N. Venkatesh, M. Baskaran, V.V.S.R. Karri, S.S. Mannemala, K. Radhakrishna, S. Goti, Fabrication and *in vivo* evaluation of Nelfinavir loaded PLGA nanoparticles for enhancing oral bioavailability and therapeutic effect, *Saudi Pharm. J.* 23 (6) (2015) 667–674.
- [35] S.S. Qi, X. Lin, M.M. Zhang, S.Z. Yan, S.Q. Yu, S.L. Chen, Preparation and evaluation of hypocrellin A loaded poly(lactic-co-glycolic acid) nanoparticles for photodynamic therapy, *RSC Adv.* 4 (75) (2014) 40085–40094.

- [36] H.D. Jung, T.S. Jang, L. Wang, H.E. Kim, Y.H. Koh, J. Song, Novel strategy for mechanically tunable and bioactive metal implants, *Biomaterials* 37 (2015) 49–61.
- [37] A. Swami, M.R. Reagan, P. Basto, Y. Mishima, N. Kamaly, S. Glavey, S. Zhang, M. Moschetta, D. Seeveratnam, Y. Zhang, J. Liu, M. Memarzadeh, J. Wu, S. Manier, J. Shi, N. Bertrand, Z.N. Lu, K. Nagano, R. Baron, A. Sacco, A.M. Roccaro, O.C. Farokhzad, I.M. Ghobrial, Engineered nanomedicine for myeloma and bone micro-environment targeting, *Proc. Natl. Acad. Sci. U. S. A.* 111 (28) (2014) 10287–10292.
- [38] X. Lin, L. Tan, Q. Zhang, K. Yang, Z. Hu, J. Qiu, Y. Cai, The in vitro degradation process and biocompatibility of a ZK60 magnesium alloy with a forsterite-containing micro-arc oxidation coating, *Acta Biomater.* 9 (10) (2013) 8631–8642.
- [39] Y. Chen, W. Zhang, M.F. Maitz, M. Chen, H. Zhang, J. Mao, Y. Zhao, N. Huang, G. Wan, Comparative corrosion behavior of Zn with Fe and Mg in the course of immersion degradation in phosphate buffered saline, *Corros. Sci.* 111 (2016) 541–555.
- [40] I. Adekanmbi, C.Z. Mosher, H.H. Lu, M. Riehle, H. Kubba, K. Elizabeth Tanner, Mechanical behaviour of biodegradable AZ31 magnesium alloy after long term in vitro degradation, *Mater. Sci. Eng. C* 77 (2017) 1135–1144.
- [41] G. Fredman, N. Kamaly, S. Spolitu, J. Milton, D. Ghorpade, R. Chiasson, G. Kuriakose, M. Perretti, O. Farokhzad, I. Tabas, Targeted nanoparticles containing the proresolving peptide Ac2–26 protect against advanced atherosclerosis in hypercholesterolemic mice, *Sci. Transl. Med.* 7 (2015), 275ra20.
- [42] ASTM G1-03, Standard Practice for Preparing, Cleaning, and Evaluating Corrosion Test Specimens, 2011, ASTM International, 2011.
- [43] ISO 8407, Corrosion of Metals and Alloys - Removal of Corrosion Products From Corrosion Test Specimens, ISO, 2009, 2009.
- [44] E.R. Shearier, P.K. Bowen, W. He, A. Drelich, J. Drelich, J. Goldman, F. Zhao, In vitro cytotoxicity, adhesion, and proliferation of human vascular cells exposed to zinc, *ACS Biomater. Sci. Eng.* 2 (4) (2016) 634–642.
- [45] B.M. Watson, T.N. Vo, A.M. Tatara, S.R. Shah, D.W. Scott, P.S. Engel, A.G. Mikos, Biodegradable, phosphate-containing, dual-gelling macromers for cellular delivery in bone tissue engineering, *Biomaterials* 67 (2015) 286–296.
- [46] H. Elmselleem, M.H. Youssouf, A. Aouniti, T. Ben Hadda, A. Chetouani, B. Hammouti, Adsorption and inhibition effect of curcumin on mild steel corrosion in hydrochloric acid, *Russ. J. Appl. Chem.* 87 (6) (2014) 744–753.
- [47] X. Liu, Q. Yang, Z. Li, W. Yuan, Y. Zheng, Z. Cui, X. Yang, K.W.K. Yeung, S. Wu, A combined coating strategy based on atomic layer deposition for enhancement of corrosion resistance of AZ31 magnesium alloy, *Appl. Surf. Sci.* 434 (2018) 1101–1111.
- [48] H.Y. Tan, E. Widjaja, F. Boey, S.C.J. Loo, Spectroscopy techniques for analyzing the hydrolysis of PLGA and PLA, *J. Biomed. Mater. Res. B* 91B (1) (2009) 433–440.
- [49] N. Rescignano, L. Tarpani, A. Romani, I. Bicchi, S. Mattioli, C. Emiliani, L. Torre, J.M. Kenny, S. Martino, L. Latterini, I. Armentano, In-vitro degradation of PLGA nanoparticles in aqueous medium and in stem cell cultures by monitoring the cargo fluorescence spectrum, *Polym. Degrad. Stab.* 134 (2016) 296–304.
- [50] J. Zimmermann, N. Jürgensen, A.J. Morfa, B. Wang, S. Tekoglu, G. Hernandez-Sosa, Poly(lactic-co-glycolic acid) (PLGA) as ion-conducting polymer for biodegradable light-emitting electrochemical cells, *ACS Sustain. Chem. Eng.* 4 (12) (2016) 7050–7055.
- [51] K. Catt, H. Li, X.T. Cui, Poly (3,4-ethylenedioxythiophene) graphene oxide composite coatings for controlling magnesium implant corrosion, *Acta Biomater.* 48 (2017) 530–540.
- [52] T. Bellezze, G. Giuliani, A. Viceré, G. Roventi, Study of stainless steels corrosion in a strong acid mixture. Part 2: anodic selective dissolution, weight loss and electrochemical impedance spectroscopy tests, *Corros. Sci.* 130 (2018) 12–21.
- [53] J. Wu, X. Lu, L. Tan, B. Zhang, K. Yang, Effect of hydron evolution by polylactic-co-glycolic acid coating on degradation rate of pure iron, *J. Biomed. Mater. Res. B* 101 (7) (2013) 1222–1232.
- [54] S. Hatamie, O. Akhavan, S.K. Sadnezhada, M.M. Ahadian, M.M. Shirolkar, H.Q. Wang, Curcumin-reduced graphene oxide sheets and their effects on human breast cancer cells, *Mater. Sci. Eng. C* 55 (2015) 482–489.
- [55] C. Karavasili, N. Bouropoulos, L. Sygellou, E.P. Amanatiadou, I.S. Vizirianakis, D.G. Fatouros, PLGA/DPPC(trimethylchitosan spray-dried microparticles for the nasal delivery of ropinirole hydrochloride: in vitro, ex vivo and cytocompatibility assessment, *Mater. Sci. Eng. C* 59 (2016) 1053–1062.
- [56] C. López-Santos, A. Terriza, J. Portolés, F. Yúbero, A.R. González-Elipe, Physiological degradation mechanisms of PLGA membrane films under oxygen plasma treatment, *J. Phys. Chem. C* 119 (35) (2015) 20446–20452.
- [57] T.I. Croll, A.J. O'Connor, G.W. Stevens, J.J. Cooper-White, Controllable surface modification of poly(lactic-co-glycolic acid) (PLGA) by hydrolysis or aminolysis I: physical, chemical, and theoretical aspects, *Biomacromolecules* 5 (2) (2004) 463–473.
- [58] X. Kong, J. Wang, L. Cao, Y. Yu, C. Liu, Enhanced osteogenesis of bone morphology protein-2 in 2-N,6-O-sulfated chitosan immobilized PLGA scaffolds, *Colloids Surf. B* 122 (2014) 359–367.
- [59] J.S. Stevens, A.C. de Luca, M. Pelendritis, G. Terenghi, S. Downes, S.L.M. Schroeder, Quantitative analysis of complex amino acids and RGD peptides by X-ray photoelectron spectroscopy (XPS), *Surf. Interface Anal.* 45 (8) (2013) 1238–1246.
- [60] A. Ganguly, S. Sharma, P. Papakonstantinou, J. Hamilton, Probing the thermal deoxygenation of graphene oxide using high-resolution in situ X-ray-based spectroscopies, *J. Phys. Chem. C* 115 (34) (2011) 17009–17019.
- [61] P. Taheri, J. Wielant, T. Hauffman, J.R. Flores, F. Hannour, J.H.W. de Wit, J.M.C. Mol, H. Terryn, A comparison of the interfacial bonding properties of carboxylic acid functional groups on zinc and iron substrates, *Electrochim. Acta* 56 (4) (2011) 1904–1911.
- [62] L.J. Gibson, The mechanical behaviour of cancellous bone, *J. Biomech.* 18 (5) (1985) 317–328.
- [63] M. Xu, H. Li, D. Zhai, J. Chang, S. Chen, C. Wu, Hierarchically porous nagelschmidtite bioceramic-silk scaffolds for bone tissue engineering, *J. Mater. Chem. B* 3 (18) (2015) 3799–3809.
- [64] Y.F. Zheng, X.N. Gu, F. Witte, Biodegradable metals, *Mater. Sci. Eng. R* 77 (2014) 1–34.
- [65] A.K. Nasution, N.S. Murni, N.B. Sing, M.H. Idris, H. Hermawan, Partially degradable friction-welded pure iron-stainless steel 316L bone pin, *J. Biomed. Mater. Res. B* 103 (1) (2015) 31–38.
- [66] D.T. Chou, D. Wells, D. Hong, B. Lee, H. Kuhn, P.N. Kumta, Novel processing of iron-manganese alloy-based biomaterials by inkjet 3-D printing, *Acta Biomater.* 9 (10) (2013) 8593–8603.
- [67] A. Agarwal, A. Kasinathan, R. Ganeshan, A. Balasubramanian, J. Bhaskaran, S. Suresh, R. Srinivasan, K.B. Aravind, N. Sivalingam, Curcumin induces apoptosis and cell cycle arrest via the activation of reactive oxygen species-independent mitochondrial apoptotic pathway in Smad4 and p53 mutated colon adenocarcinoma HT29 cells, *Nutr. Res.* 51 (2018) 67–81.
- [68] Y. Qi, H. Qi, Y. He, W. Lin, P. Li, L. Qin, Y. Hu, L. Chen, Q. Liu, H. Sun, Q. Liu, G. Zhang, S. Cui, J. Hu, L. Yu, D. Zhang, J. Ding, Strategy of metal-polymer composite stent to accelerate biodegradation of iron-based biomaterials, *ACS Appl. Mater. Interfaces* 10 (1) (2018) 182–192.
- [69] Z. Wang, R. Qiao, N. Tang, Z. Lu, H. Wang, Z. Zhang, X. Xue, Z. Huang, S. Zhang, G. Zhang, Y. Li, Active targeting theranostic iron oxide nanoparticles for MRI and magnetic resonance-guided focused ultrasound ablation of lung cancer, *Biomaterials* 127 (2017) 25–35.
- [70] W. Lin, L. Qin, H. Qi, D. Zhang, G. Zhang, R. Gao, H. Qiu, Y. Xia, P. Cao, X. Wang, W. Zheng, Long-term in vivo corrosion behavior, biocompatibility and bioresorption mechanism of a bioresorbable nitrided iron scaffold, *Acta Biomater.* 54 (2017) 454–468.
- [71] M. Hrubovčáková, M. Kupková, M. Džupon, M. Giretová, Ľ. Medvecký, R. Džunda, Biodegradable polylactic acid and polylactic acid/hydroxyapatite coated iron foams for bone replacement materials, *Int. J. Electrochem. Sci.* 12 (2017) 11122–11136.